ELSEVIER

J. Non-Newtonian Fluid Mech. 134 (2006) 56–76

Journal of Non-Newtonian Fluid Mechanics

www.elsevier.com/locate/jnnfm

Stabilised computations for viscoelastic flows under compressible implementations☆

F. Belblidia, I.J. Keshtiban, M.F. Webster*

Institute of Non-Newtonian Fluid Mechanics, Computer Science Department, Digital Technium, University of Wales Swansea, Swansea SA2 8PP, UK

Received 12 May 2005; received in revised form 11 November 2005; accepted 1 December 2005

Abstract

We analyse and contrast different stabilisation methodologies embedded within a time-marching incremental pressure-correction formulation. Numerical solutions are presented for an Oldroyd-B model under compressible implementations, considering flow through a planar four-to-one abrupt contraction. Various alternative stabilisation strategies and their combinations are analysed to hone the response of the base hybrid finite element/volume implementation. To reflect the stabilised properties of each scheme, the study interrogates levels of stable Weissenberg number (*We*) solution. Results indicate that most improvement has been encountered with a *Strain-Rate Stabilisation* scheme, where critical *We*-levels have more than doubled above neutral variants, while stress peaks levels have been constrained. Here, differed-correction characterises temporal error norm stress behaviour and the nature of the re-entrant corner stress singularity. At a selected *We*-level and under a specific flow setting, all scheme variants have produced similar salient-corner vortex behaviour, predicting vortex reduction under increasing *We*. In contrast, lip-vortex features are found to be significantly affected by the particular re-entrant corner treatment applied. When present, lip vortices grow with increasing *We*. Relaxation of the incompressible constraint points to important numerical anomalies, present under certain discretisations.

Keywords: Strain-rate stabilisation; High-order incremental pressure-correction; Oldroyd-B; Planar contraction; Critical Weissenberg number; Vortex activity; Low Mach number; Compressible

1. Introduction

The motivation behind this study is to compare and contrast some stabilisation methodologies for viscoelastic flow around the incompressible limit. That is under the platform of a fractional-staged splitting of equations and a hybrid finite element/finite volume (*fe/fv*) spatial discretisation. We introduce for the first time *incremental pressure-correction* (*PC*) formulations within the viscoelastic context. Novelty lies in our investigation of highly elastic solutions and stabilised computations for slightly compressible and incompressible flows. The efficiency of *PC* formulations advocates this choice over coupled alternatives, particularly for large-scale problems. Our prior work under *PC* and *fe/fv* has covered complex viscoelastic incompressible [1] and compressible flows [2,3], and has been extended to some transient flows [4]. Here, we continue on this theme, considering steady-state Oldroyd-B model solutions in planar 4:1 abrupt contraction flows, taking the equation of state for compressible liquids as the celebrated Tait equation. For suitable background, one may refer to many contributions in the incompressible literature, being well covered by three review articles of Keunings [5], Baaijens [6] and Walters and Webster [1].

Fresh issues dealt with in the present study involve: (i) the stabilisation of *PC*-schemes in application to the coupled velocity–pressure–stress system; (ii) the improved satisfaction of extended LBB compatibility conditions within the spatial representation; and (iii) some miscellaneous stabilisation aspects particular to the stress equation.

Under the *first issue*, we appeal to new theoretical findings in this area associated within the coupled velocity–pressure system, strengthening the links between fractional-staged equations and enhancing temporal accuracy thereby. Codina and Zienkiewicz [7] have established the association of the stabilisation parameter of the *Galerkin-Least-Squares* (GLS) method with the proper choice of time-step in a *PC*-approach [7]. This is achieved through stabilisation factors, introduced into their *Characteristic-Based Split* (*CBS*) fractional-staged approach. Though our present schemes depart from the *CBS*-split in retaining incremental pressure terms throughout the momentum-

☆ Paper presented at the AERC 2005 Conference held in Grenoble, France.

* Corresponding author. Tel.: +44 1792 295656; fax: +44 1792 295708.
E-mail address: M.F.Webster@swansea.ac.uk (M.F. Webster).

0377-0257/$ – see front matter © 2005 Elsevier B.V. All rights reserved.
doi:10.1016/j.jnnfm.2005.12.003

balance phase, the introduction of their stabilisation factors is related to our earlier work on *Time-Step Relaxation/Scaling* (see [2]). Similarly in [8], the new incremental *PC*-structure is introduced and the necessity of satisfying the inf-sup (LBB) conditions is confirmed, if superior temporal error bounds are to be realised. Admissible trial spaces and specific incremental-*PC* schemes are advocated with three time-levels, reflecting second-order accuracy in time. The multi-time level strategy ties further implicitness into the system and stronger enforcement of continuity satisfaction through time, theoretically strengthening convergence and stability properties of the algorithm thereby. This has led us to identify a stabilisation strategy base upon *Time-Step Relaxation/Scaling*. In the high Weissenberg number (*We*) regime seeking steady-state solutions, we discover that *Time-Step Stabilisation* is not a particularly strong stabilisation influence, contrary to our previously findings at low-*We* [2]. True-transients may reveal more here.

The *second issue* involves enhancing the compatibility of function spaces. This entails the improvement in quality of the velocity-gradient representation and the appending of an elliptic dissipation function to the momentum balance sub-system. Emerging as a core component to the current work, here we investigate to distinct advantage a particular *Strain-Rate Stabilisation* technique: the coupling together of stress-splitting (DEVSS-type) with a localised form of velocity-gradient representation. The precise details on implementation of this scheme are outlined in Section 3.1.

The *third* stabilisation issue is related to the difficulties encountered within the computation of stress itself, via the constitutive equation. This gives rise to such miscellaneous aspects as accommodating for cross-stream diffusion, capturing discontinuities and steep stress gradients. Implicit differential constitutive equations invariably display hyperbolic character and amalgamate the system into one of mixed-type: hyperbolic/parabolic (unsteady) or hyperbolic/elliptic (steady). The resulting stress solution often reflects large components in elastic extra-stress, which may support steep/discontinuous stress gradients in the vicinity of a singularity. Under such circumstances, particular treatment is necessary for effective discretisation, which would also encompass some form of upwinding procedure. Sharp discontinuity capturing procedures stabilise the solution locally about singular field locations, to suppress non-physical oscillations. In this respect, Aboubacar and Webster [9] employed discontinuity capturing, based on a *Reduced Corner Integration* technique applied in *finite-volume* cells adjoining the re-entrant corner (six-point Newton–Cotes rule reduced to three-point rule). This technique is revisited within the present study. The rationale behind such a treatment lay in reflecting low-order local approximation, tightly capturing sharp gradients, whilst suppressing propagation of numerical noise away from singular solution zones.

Through the proposed alternative stabilisation procedures, we are able to access larger levels of stable *We*-solution. This presents us with novel solution features to report, covering mildly compressible and incompressible regimes and in terms of vortex activity, stress field structure, and cross-stream solution representation. We may consider the specific effect that inclusion of compressibility can have, contrasting this against its incompressible counterpart, notably through vortex activity.

2. Governing equations

The governing equations for viscoelastic flow are represented by those for mass conservation and momentum transport, in conjunction with equations of state for stress and density (compressible flow). The non-dimensional form of continuity and momentum balance equations for isothermal compressible creeping flow may be expressed as

$$\frac{\partial \rho}{\partial t} + \nabla \cdot (\rho \mu) = 0, \tag{1}$$

$$Re\, \rho \frac{\partial u}{\partial t} = \nabla \cdot \left(2\mu_s^* D + \mu_s^* \left(\frac{\kappa}{\mu_s^*} - \frac{2}{3} \right) (\nabla \cdot u) \delta_{ij} + \tau \right) - \nabla p, \tag{2}$$

where ρ, u, p and τ represent density, velocity, hydrodynamic pressure and extra-stress, respectively. Here, $2D_{ij} = (L_{ij} + L_{ij}^{\mathrm{T}})$ and $L^{\mathrm{T}} = \nabla u$. We shall have need to refer to various viscosity material parameters of μ, μ_e and μ_s, to represent factors of total, polymeric-fraction and solvent-fraction, respectively, where $\mu = \mu_e + \mu_s$. Henceforth, we refer to $\mu_e^* = \mu_e/\mu$ and $\mu_s^* = \mu_s/\mu$. κ is a generalised factor that mimics the role of bulk viscosity. Bulk viscosity arises as a consequence of active rotational and vibrational modes at the polyatomic molecular level, relevant in compressible gas or granular matter flow (see [10]). Note, the effect of variation in bulk viscosity (κ) on scheme stabilisation is largely withheld to a more detailed treatise on this particular aspect [11]. For convenience, we introduce $\bar{\tau}_s$ as being the augmented solvent stress referenced within the momentum transport equation:

$$\bar{\tau}_s = \left(2\mu_s^* D + \mu_s^* \left(\frac{\kappa}{\mu_s^*} - \frac{2}{3} \right) (\nabla \cdot u) \delta_{ij} \right). \tag{3}$$

The Oldroyd-B constitutive equation is given by

$$\tau + We \frac{\partial \tau}{\partial t} = -We\, u \cdot \nabla \tau + We(L \cdot \tau + \tau \cdot L^{\mathrm{T}}) + 2\mu_e^* D. \tag{4}$$

The Reynolds number (*Re*) and Weissenberg number (*We*) are appropriate non-dimensional group numbers, defined according to convention as

$$Re = \frac{\hat{\rho} \hat{U} l}{\mu}, \qquad We = \frac{\lambda \hat{U}}{l}, \tag{5}$$

where $\hat{\rho}$, μ and λ denote selected reference density, total viscosity and relaxation time; $\hat{U}$, l are characteristic velocity and length scales (channel exit half-width) of the flow. By convention, for the 4:1 contraction flow, a characteristic velocity scale for incompressible flow may be assumed as the average taken over channel outlet. Generally, this is calculated via the continuity equation from fully developed outlet flow considerations. For incompressible flow, density is constant and inlet mass flow-rate may be calculated, from imposed boundary conditions. In contrast for compressible flow, density at the inlet is a dependent

variable, and for equitable comparison, we have again selected the velocity scale, of the equivalent steady state for flow-rate incompressible flow, as above.

To close the set of equations, it is necessary to introduce an equation of state to link density to pressure. In this regard, the Tait equation of state (see [3]) has been extensively employed in polymer processing to describe the relationship between density, pressure and temperature, viz.:

$$\tilde{P} + B = B\rho^m, \quad \text{where augmented pressure}$$
$$\tilde{P} = P - \tfrac{1}{3}\mathrm{tr}(\tau + \bar{\tau}_s). \tag{6a}$$

Here B represents a non-dimensional shift for pressure and m a dimensionless power-index. Assuming isentropic conditions, we gather:

$$\frac{\partial \tilde{P}}{\partial \rho} = \frac{m(\tilde{P} + B)}{\rho} = c^2, \tag{6b}$$

where c is the derived speed of sound in the fluid (see [3] for further details). For clarity, henceforth we discard yet imply (*) notation on viscosity fractions and (∼) notation on pressure. At this point, we may define the Mach number, $Ma = u/c$ being the ratio of fluid velocity to the speed of sound.

The compressible version of the algorithm with $\rho \neq$ constant ($Ma > 0$) is the more general classification, collapsing to the incompressible form with $\rho =$ constant ($Ma = 0$), for which $\nabla \cdot u \equiv 0$ in Eq. (3). This limit may be emulated practically by setting the Tait parameter pairing (m, B) to high levels, asymptoting to $Ma \approx 0$ ($\kappa = 0$). From a numerical perspective, introducing compressibility conveys residual from the continuity equation into the momentum equation, whereupon residuals are minimised simultaneously. Thereby, violation of local mass conservation may be reduced. We may recall in our earlier studies [3], the improved stabilisation characteristics of the compressible above the incompressible algorithm, in terms of temporal convergence history and reduction of the associated bandwidth between variables. Here, we concentrate almost entirely upon the incompressible limiting setting (either $Ma = 0$ or $Ma \approx 0$). Nevertheless, we finally provide some detail for the slightly compressible flow setting ($Ma = 0.1$, $\kappa = 0$), covering vortex behaviour and comparative scheme performance in a separate appendix.

3. Numerical method

Background detail on the time-stepping scheme, devoid of incremental *PC*, compressibility and differed-correction, may be found in our precursor studies [1,9]. For the sake of completeness, in this section we recap on the key new aspects involved. This is a semi-implicit pressure-correction scheme of *incremental* form attracting second-order accuracy. The time and operator splitting for this algorithm leads to a three-staged fractional structure per time-step cycle. In this formulation, the momentum and constitutive equations are solved to provide an auxiliary velocity (u^*) and stress (*stage-1*) with back-time reference in pressure ($2p^n - p^{n-1}$); a pressure calculation (*stage-2*) emerges via the continuity constraint on velocity; and finally (*stage-3*), mass conservation is enforced on velocity via the contribution from the pressure increment. The forward time reference is affected through $\theta(p^{n+1} - p^n)$ for which $\theta = 0.5$ constructs Crank–Nicolson splitting.

In order to deal with non-linear terms at stage-1, a two-step Lax–Wendroff predictor-corrector scheme is adopted. This avoids solving non-linear terms of implicit form and falls into a predictor (*stage-1a*) and corrector (*stage-1b*) structure. The diffusion term in the momentum equation is treated in a semi-implicit manner, enhancing stability, whilst avoiding the computational overhead of a fully implicit alternative. The compact semi-discrete form of this scheme may be represented as follows, with indication of where *Strain-Rate Stabilisation* terms will arise:

- *Stage-1a*:

$$\frac{2\mathrm{Re}}{\Delta t}\rho^n\left(u^{n+1/2} - u^n\right) - \nabla\cdot\left(\bar{\tau}_s^{\,n+1/2} - \bar{\tau}_s^{\,n}\right) = \nabla\cdot\left(\bar{\tau}_s^{\,n} + \tau^n\right) - \boxed{\nabla\left(2p^n - p^{n-1}\right)} + \boxed{SRS\text{ - term}} \tag{7}$$

$$\frac{2}{\Delta t}(\tau^{n+1/2} - \tau^n) = \left[-u\cdot\nabla\tau + \frac{1}{We}(2\mu_e D - \tau) + L\cdot\tau + \tau\cdot L^{\mathrm{T}}\right]^n \tag{8}$$

- *Stage-1b*:

$$\frac{\mathrm{Re}}{\Delta t}\rho^n\left(u^* - u^n\right) - \nabla\cdot\left(\bar{\tau}_s^{\,*} - \bar{\tau}_s^{\,n}\right) = \nabla\cdot\left(\bar{\tau}_s^{\,n} + \tau^{n+1/2}\right) - \boxed{\nabla\left(2p^n - p^{n-1}\right)} + \boxed{SRS\text{ - term}} \tag{9}$$

$$\frac{1}{\Delta t}(\tau^{n+1} - \tau^n) = \left[-u\cdot\nabla\tau + \frac{1}{We}(2\mu_e D - \tau) + L\cdot\tau + \tau\cdot L^{\mathrm{T}}\right]^{n+1/2} \tag{10}$$

- *Stage-2*:

$$\boxed{\frac{1}{c^2\Delta t^2}(p^{n+1} - p^n)} - \theta\nabla^2(p^{n+1} - p^n) = -\frac{1}{\Delta t}\nabla\cdot(\rho^n u^*) \tag{11}$$

- *Stage-3*:

$$\frac{Re}{\Delta t}\rho^{n+1}(u^{n+1} - u^*) = -\theta\nabla(p^{n+1} - p^n). \tag{12}$$

In the above equations, once spatial discretisation has been introduced, the *Strain-Rate Stabilisation* term takes a form $\int_\Omega \phi_i 2\alpha\mu_s \nabla\cdot(D - D_c)^n \,\mathrm{d}\Omega$, over domain Ω with weighting functions $\phi_i(x)$. Then, D represents the discontinuous rate-of-deformation under *fe*-approximation, and D_c its recovered

equivalent based on localised velocity-gradient recovery procedures [12] (see Section 3.1). The superscript (n) denotes the time level and Δt the time-step.

For spatial discretisation, Carew et al. [13] employed a Galerkin *fe*-approximation for velocity and pressure, with SUPG-weighting on stress. Alternatively and more recently in Wapperom and Webster [14], we have adopted a novel hybrid *fe/fv* scheme, based on a Galerkin *fe*-approximation for mass-momentum balance, and a cell-vertex *fv*-form for stress computation. One may find close similarity between this scheme and the so-called 4×4 stress sub-elements, introduced by Marchal and Crochet [15]. The choice of *fe*-element in [14] is a six-node (P2P1) element, with quadratic interpolation for velocity and linear for pressure based on vertex nodes (see Fig. 1 in [9]). The *fe*-grid may be utilised as a platform for the *fv*-grid, from which *fv*-control volumes are constructed. Each *fv*-cell is composed of four sub-triangles, formed by connecting the mid-side nodes of the parent element. Stress variables are located at the vertices of the *fv*-cells and may be used directly as *fe*-nodal values without interpolation. Selecting this type of element supports some important features. For the calculation of velocity at low Reynolds numbers, employing a quadratic velocity interpolation is well suited to capturing flow patterns near solid boundaries. This enhances the quality of velocity-gradient representation, which has a major impact upon scheme performance within stress boundary layers. The parent *fe*-element structure has advocated a second-order recovery-type technique (see [12]). In comparison, Aboubacar and Webster [9] have observed that linear-form elements (sub-cell) for stress are more suitable in damping numerical noise, and hence, prove more successful in attaining higher *We*-solutions in some flows (recall the experience of Basombrio et al. [16] likewise, for quadratic to linear stress interpolation results). Our emerging hybrid *fe/fv*-scheme (named *CT3*) enjoys improved quality of velocity gradients, obtained via recovery and applied over parent *fe*-elements, with linear-form elements for stress over sub-cells.

Here, we briefly describe our *fv*-discretisation employed for stress (*CT3*), upon which additional stabilisation strategies are constructed namely: *Time-Step Stabilisation*, *Reduced Corner Integration*, and *Strain-Rate Stabilisation* (in figures represented as TSS, *RCI* and *SRS*, respectively). The cell-vertex *fv*-scheme applied to stress is based upon a *fluctuation distribution* upwinding technique, that distributes control volume residuals to provide nodal solution updates. We refer the reader to previous studies for the properties of such a class of schemes in computing steady-state solutions [1,9], and true-transient viscoelastic solutions [4]. Concisely, the constitutive equation is presented using convective flux (R) and source (Q) terms, viz.:

$$\frac{\partial \tau}{\partial t} = -R + Q, \tag{13}$$

$$R = u \cdot \nabla \tau, \qquad Q = \frac{1}{We}(2\mu_e D - \tau) + L \cdot \tau + \tau \cdot L^{\mathrm{T}}. \tag{14}$$

To extract the discrete flux, source and time-terms employed, and to construct the nodal-update equations for a particular scalar stress-component, τ_1, we integrate Eq. (13) over triangular sub-cell control volumes. We use two such control volumes: each *fv*-subcell T_1 surrounding node l (Ω_l), and its median-dual-cell (*MDC*) associated with node l (Ω_l) (see Fig. 1 in [9]). The subscripts and superscripts, T and *MDC*, express terms evaluated over Ω_T and Ω_l about node l, respectively. A discretised scalar nodal form of Eq. (13) over each triangle T can be expressed as

$$\left(\delta_T \alpha_l^T \Omega_T + \frac{1}{3}\Omega_T\right) \frac{\tau_l^{n+1} - \tau_l^n}{\Delta t} = \delta_T \alpha_l^T (R_T + \beta_1 Q_T) + \delta_{MDC}(\beta_2 R^l_{MDCT} + Q^l_{MDCT}), \tag{15}$$

where α_l^T represents the *fluctuation distribution* coefficient. A nodal equation update, pertinent for node l, is obtained via ensemble contributions from all triangles surrounding node l. The terms (R_T, Q_T) and (R^l_{MDC}, Q^l_{MDC}) correspond to flux and source components over the *fv*-triangle T and *MDC*-zone, respectively. Parameters δ_T and δ_{MDC} dictate flux-source weighting and different scheme options, as do Boolean factors, β_1, β_2 (taken as unity). As such in [14], we retained parameter $\delta_T = \xi$ if $|\xi| \leq 1$ and 1 otherwise. Here, $\xi = 3\,We(a/h)$, with a the magnitude of the average advection velocity per *fv*-cell and h the square root of the area of the *fv*-cell. In addition, for the parameter δ_{MDC}, we select $\delta_{MDC} = 1 - \delta_T$.

3.1. Strain-rate stabilisation scheme

The mathematical analysis of Stokes flow indicates that the approximation spaces for velocity and pressure must a priori satisfy a compatibility condition known as the inf-sup or LBB condition (see [17]). Furthermore for viscoelastic flows, the addition of a weak-form stress constitutive equation, imposes supplementary compatibility conditions on admissible interpolation spaces for velocity gradients ($S(\nabla u) \subset S(\tau)$) (see [18,19], re DG-schemes). Nevertheless, extended inf-sup type conditions for such flows are less well developed. The numerical consequence of deviation from such conditions appears in the form of numerical oscillations and poor stability response. The order of accuracy in representation for velocity gradients plays a significant role in the satisfaction of LBB conditions. To this end, several approaches have been developed to extract velocity gradients at finite elements nodes. One scenario is to employ a weighted-residual approximation on the whole computational domain to gather velocity gradients as primary variables (as in DEVSS-type schemes [17]). An alternative approach is to employ localised superconvergent patch-recovery methods to compute velocity gradients, see [20]. Matallah et al. [12] concluded that, utilising recovery in this manner, may yield an accurate and stable implementation. Localised approximations of this form were shown to be equally as competitive to other global weighted-residual alternatives, irrespective of the stress-splitting formulations adopted (DEVSS-variants, DEVSS/SUPG and DEVSS/DG, see [12,21–23]). In [12], it was concluded that the single most important factor was the treatment of velocity gradients (weak or strong form), as opposed to the stress-splitting per se.

In addition, the presence of an elliptic operator, introduced via operator-splitting has been found to considerably enhance LBB satisfaction for viscoelastic flows. This has been implemented in various forms of EVSS (stress-splitting) schemes. Guénette and Fortin [24] introduced DEVSS in order to modify and generalise the EVSS scheme. Here, an elliptic smoothing function may be derived, based on the residue between the continuous and discontinuous spatial representations for the solvent stress term. Similarly we have defined a generalised differed-correction term within the weak-form weighted-residual expression for momentum, gathered at time level t^n:

$$\int_{\Omega} \frac{\partial \phi_i}{\partial x_k}(2\alpha\mu_s(D - D_c))^n \, d\Omega \tag{16}$$

which would appear in fully discrete form as the last term of Eqs. (7) and (9). The discontinuous form, D emerges via the *fe*-approximation (here on triangles over domain Ω, quadratic functions $\phi_k(x)$, $k = 1, \ldots, 6$; nodal reference). The representation of continuous form, D_c, is the key point here. Equivalently, within DEVSS, for example, this is derived based on global weighted-residual procedures demanding further separate and additional equations, incurring significant computational overhead accordingly. Alternatively, the recovery approach achieves the same primary variable extraction for velocity gradients based on a localised treatment. To explain the detail, we assume *fe*-quadratic piecewise-continuous interpolation for velocity components, $u_i(x,t)$ over the parent-triangular tessellation $\{\sum_{e_k} \Omega_{e_k} = \Omega\}$, with implied repeated indicial summation convention:

$$u_i(x|_{x \in \Omega_e}, t^n) = \phi_k(x) U_i(t^n)_k \quad | \quad i = 1, 2; \quad \text{on } \Omega_e, \ k = 1, \ldots, 6. \tag{17}$$

From this evaluation, we may identify an expression for velocity gradients at nodal points, multiple-valued on the domain:

$$G_{ij}(x|_{x \in \Omega_e}, t^n)_e = \frac{\partial \phi_k(x)}{\partial x_j} U_i(t^n)_k \quad | \quad i, j = 1, 2; \quad \text{on } \Omega_e, \ k = 1, \ldots, 6. \tag{18}$$

To construct a recovered continuous representation, we extract single-valued nodal quantities for velocity gradients, say at global node k, position x_k, with proper weighting factors w_{e_k}:

$$G_{ij}^{\mathrm{Rec}}(x_k, t^n) = \sum_{e_k}^{\mathrm{TES}\ \Omega_{e_k}} w_{e_k} G_{ij}(x_k, t^n)_{e_k} | \mathrm{TES}\ \Omega_{e_k}, \quad \text{total elements shared at node } k, \text{ each element } \Omega_{e_k}. \tag{19}$$

From this, the recovered continuous representation is

$$G_{ij}^{\mathrm{Rec}}(x|_{x \in \Omega_e}, t^n) = \phi_k(x) G_{ij}^{\mathrm{Rec}}(t^n)_k \quad | \quad i, j = 1, 2; \quad \text{on } \Omega_e, \ k = 1, \ldots, 6. \tag{20}$$

Options arise for weighting factors w_{e_k} and elemental contributions of velocity gradients. We have chosen $G_{ij}^{\mathrm{Rec}}(t^n)_k$ as the single-valued area-contribution from each sharing *fe*-triangle e_k containing node-k. An alternative choice would be to suitably sample from multiple nodal values with linear-contributions (see [20]). The weighting factors, w_{e_k}, must accommodate accordingly for both the number of such contributions and their proportionate influence on the result (area/linear size relative proportions). It is for this reason that reasonably regular spatial distributions are to be preferred to avoid distortion across complex flow zones in particular.

The parameter α in Eq. (16) deserves some mention as this adopts the role of an adjustable scalar parameter on μ_s, an optimal setting of which is gathered from empirical observation as extra-stress compatible: $\alpha = \mu_e/\mu_s$. Locally adaptive alternatives may also suggest themselves, see [21,22]. For an equivalent auxiliary viscosity to our $\alpha\mu_s$ and with the XPP-model, Verbeeten et al. [25] adopted the form $\bar{\eta} = \sum_i^M G_i \lambda_i$, where $(G,\lambda)_i$ represents the (plateau modulus, relaxation time)$_i$ per mode i, with M the number of modes.

In summary under the study of *Strain-Rate Stabilisation*, we merge some of these constructive ideas in calling upon the stress-splitting of Guénette and Fortin [24] with the deferred-correction term, use the localised recovery of velocity gradients for D_c, and employ the same for stress-equation coefficients dependent upon velocity gradients.

4. Problem description and solution strategy

In the present study, the creeping flow of an Oldroyd-B fluid through a planar 4:1 abrupt contraction is chosen as the test-problem. Practically, we can neglect momentum-convection and adopt $Re = O(10^{-2})$. This is widely recognised as a valuable benchmark to assess stability, accuracy and convergence properties, particularly at elevated levels of *We*. Such a non-smooth flow, poses a stress singularity at the re-entrant corner and a downstream-wall stress boundary layer to resolve, with provocative trends to cover in vortex behaviour and stress-field development. At the inlet, transient analytical boundary conditions are imposed on velocity and stress, following Waters and King (see [13]), as illustrated schematically in Fig. 1a. Viscosity fractions are chosen by common convention as: $\mu_e = 8/9$ and $\mu_s = 1/9$.

Pursuing steady-state solutions for both incompressible and compressible flows simulated through a compressible numerical algorithm (Eqs. (7)–(12)), optimal properties are sought in achieving unpolluted solutions at elevated critical levels of *We* (We_{crit}) for each stabilisation scheme attempted: *Time-Step Stabilisation*, *Reduced Corner Integration* and *Strain-Rate Stabilisation*. We view stress profiles, stress and pressure field plots up to We_{crit}, around the contraction zone and along the downstream-wall. We chart solutions through the boundary layer, and structures in salient-corner and lip-vortices.

We have considered two alternative solution continuation strategies. One, more stringent, of *true-time* evolution from rest at any appointed *We*-level (adjustment in time). The second follows the more conventional *incrementation* (continuation) in *We* itself (say in steps of 0.1), stepping through a series of *We* steady-state solutions (a perturbation approach). Through either solution approach, a steady state is acknowledged by satisfying a terminating preset temporal-solution increment-tolerance (set typically as $O(10^{-7})$). Under the continuation approach, We_{crit}

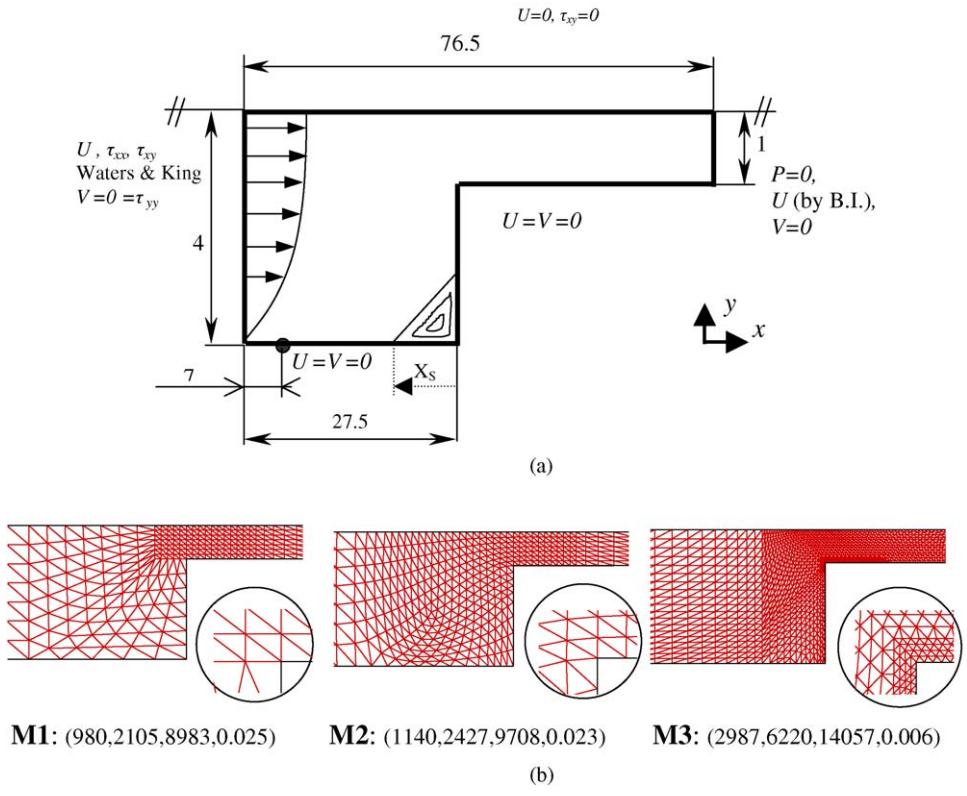

Fig. 1. Contraction flows: (a) schema, (b) mesh refinement M1–M3 around contraction (elements, nodes, d.o.f., r_{min}).

is the largest value of incremented *We* for which a stable solution could be extracted prior to scheme divergence.

5. Numerical results

We begin with a general overview and snapshot of our basic findings, as tabulated in Table 1 under limiting incompressible flow conditions ($Ma = 0.0$ and $Ma \approx 0.0$) across each stabilisation scheme, based on We_{crit} and first normal stress-peak ($N_1 = \tau_{xx} - \tau_{yy}$) levels. With *Strain-Rate Stabilisation* implementation, significant elevation is observed beyond We_{crit} levels for the *CT3*-scheme. *Time-Step Stabilisation* solutions replicate the characteristics of *CT3*-solutions around We_{crit}-levels. Stress-peak levels confirm agreement in solution at each *We*-stage reached, with rise as *We* increases for each scheme. *Reduced Corner Integration* captures steep stress gradients sharply and has larger stress-peak values compared to alternative schemes. In contrast, *Strain-Rate Stabilisation* reduces stress-peak levels significantly. Comparatives for combinations of various stabilisation strategies are also presented in Table 1.

5.1. Spatial and temporal convergence

We have conducted extensive mesh refinement studies of direct relevance, both here and elsewhere [2,23,26,27], covering detailed results on both incompressible and compressible flows. For example, we have demonstrated in [3], that there is little apparent loss of spatial accuracy incurred through our compressible implementation, as compared to its incompressible counterpart in cavity flows. For *CT3*-scheme, in [27], for transient viscoelastic problems, spatial accuracy was shown to reach a second-order, and in excess of this for steady model problems [23]. Furthermore, temporal convergence-rates to steady state for the compressible interpolation-form have been shown to improve upon those for the incompressible version [2,26].

Table 1
Incompressible setting ($Ma = 0$ and $Ma \approx 0$): We_{crit} and principal stress-peak N_1, various schemes

	$Ma = 0$						$Ma \approx 0$			
	Alone			Combination			Alone			Combination
	CT3 (TSS)	*RCI*	*SRS*	TSS + *RCI*	*RCI* + *SRS*	TSS + *RCI* + *SRS*	*CT3*	*RCI*	*SRS*	*RCI* + *SRS*
Critical *We*	2.8	3.0	5.9	3.5	6.1	6.4	2.0	3.3	5.4	6.3
Peak N_1 at We_{crit}	91.5	105.9	133.4	85.1	157.8	171.2	102.2	194.0	103.1	154.0
N_1 at $We = 2.0$	81.3	67.2	77.5	58.2	72.9	72.9	102.2	116.2	70.3	69.5

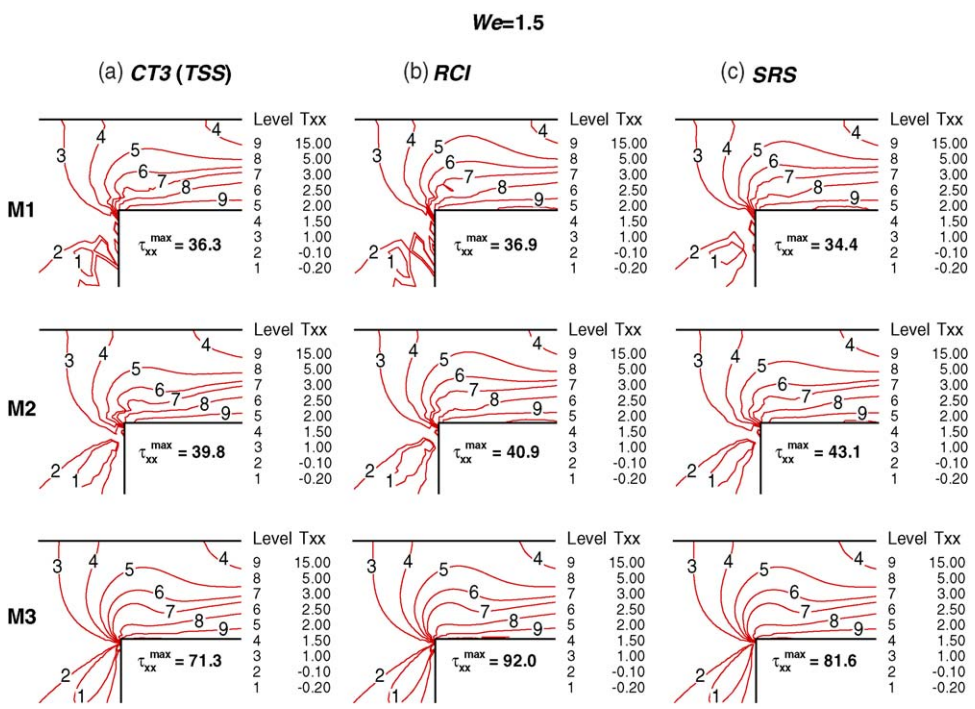

Fig. 2. $Ma = 0$ spatial convergence trends, τ_{xx}-contour fields: (a) *CT3*, (b) *RCI* and (c) *SRS* schemes; $We = 1.5$, mesh M1 (top), M2 (middle), M3 (bottom).

For the range of schemes of current interest, spatial accuracy is conducted via the three levels of mesh refinement (M1, M2 and M3 of Fig. 1b), under $Ma = 0$ and true-time continuation. Parameter selection is taken consistent with the temporal convergence analysis below, with a fixed time-step of $\Delta t = 10^{-4}$ and $We = 1.5$. Fig. 2 illustrates τ_{xx}-contour field plots around the contraction zone plotted at the same stress levels for the various scheme variants and meshes. The characteristics of mesh convergence are displayed with consistent trends across all schemes as the mesh is progressively refined, through M1 to M2 to M3[1]. Numerical noise present in these most sensitive solution fields on the coarser meshing (M1) is shown to be identified and practically removed by arriving at the finest mesh (M3). This noise is most prominent about/above the re-entrant corner and just beyond into the stress boundary layer region. τ_{xx}-stress peak levels demonstrate a consistency through refinement for each scheme, with a common comparable trend of sharpness across schemes, rising with refinement as anticipated. Table 2 provides detailed pointwise representative samples for τ_{xx}-values, across meshes and schemes. Numerical accuracy achieved through mesh M3 is also highlighted and judged independently against the literature in Fig. 14, by contrasting salient-corner vortex characteristics (intensity and size) against those computed through a very fine discretisation of Alves et al. [28], see on to Section 6.

Furthermore, Fig. 3 illustrates the associated temporal convergence tolerances for stress across scheme and mesh refinement for $\Delta t = 10^{-4}$ at $We = 1.5$. Overall, the same temporal convergence trends are observed across mesh and scheme in stress (likewise in velocity and pressure). Under the finest mesh M3, testing across schemes reveals that *Strain-Rate Stabilisation* gathers the most rapid ultimate convergence rate, followed by that under *Reduced Corner Integration* (see Fig. 3d).

Temporal rates of convergence under *Strain-Rate Stabilisation* and various solution components are illustrated in Fig. 4 at $We = 1.5$, through different levels of time-step ($\Delta t = 5 \times 10^{-4}$, 10^{-4}, 5×10^{-5}) on the finest mesh M3. Under the smallest time-step selected, where spatial discretisation error is minimal, less time is required than with the other time-step settings to attain the specified tolerance level, with more rapid early convergence

Table 2
$Ma = 0$ setting: τ_{xx}-values at sampled locations, various schemes and meshes, $We = 1.5$

	Sampling point position	*CT3*	*RCI*	*SRS*
M1				
Core-channel	X_{corner} −5, $Y = 2$	0.0210	0.0211	0.0210
Centreline	X_{corner} −5, $Y = 4$	0.0136	0.0131	0.0146
	X_{corner} +20, $Y = 4$	−0.0206	−0.0206	−0.0218
M2				
Core-channel	X_{corner} −5, $Y = 2$	0.0212	0.0213	0.0212
Centreline	X_{corner} −5, $Y = 4$	0.0124	0.0125	0.0123
	X_{corner} +20, $Y = 4$	−0.0194	−0.0194	−0.0201
M3				
Core-channel	X_{corner} −5, $Y = 2$	0.0212	0.0213	0.0212
Centreline	X_{corner} −5, $Y = 4$	0.0124	0.0125	0.0123
	X_{corner} +20, $Y = 4$	−0.0194	−0.0194	−0.0201

[1] One may infer from this evidence in similarity of trends, that the order of accuracy, established earlier for *CT3*-scheme in [23], will replicate across all variants.

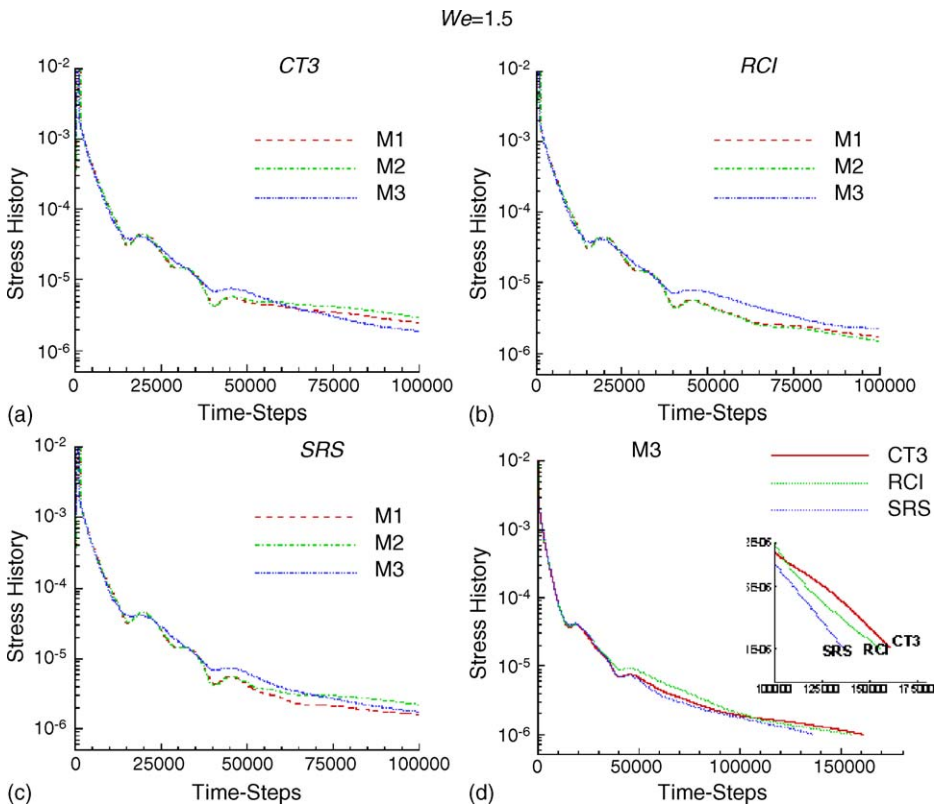

Fig. 3. $Ma = 0$ temporal convergence patterns for stress with mesh refinement; $We = 1.5$, $\Delta t = 10^{-4}$: under schemes (a) *CT3*, (b) *RCI* and (c) *SRS*; (d) across schemes M3-mesh.

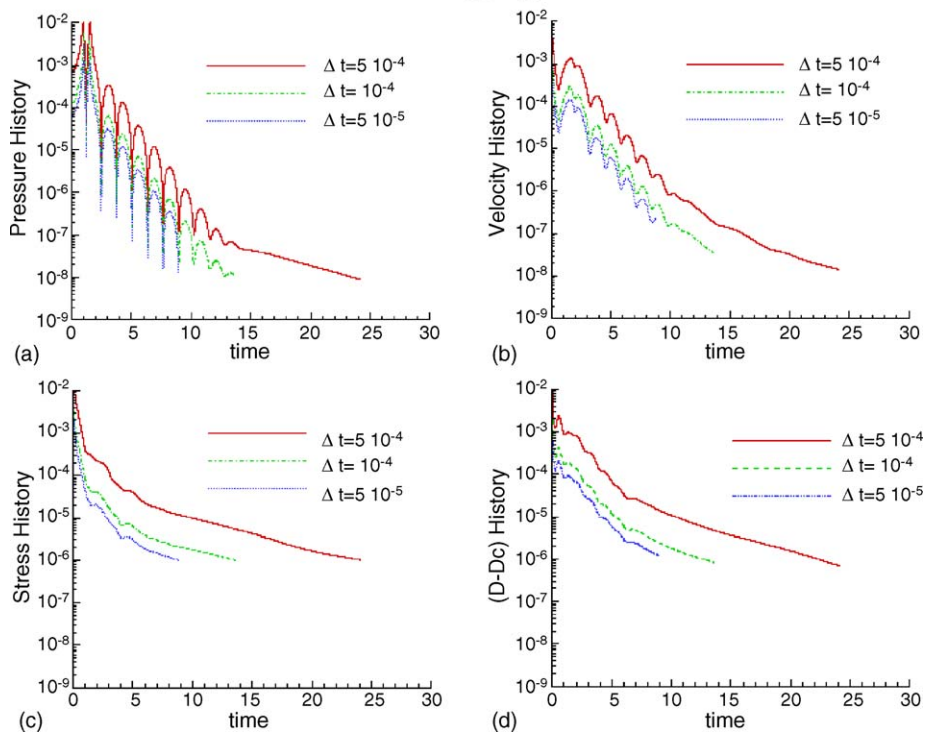

Fig. 4. $Ma = 0$ temporal convergence patterns with temporal refinement; $We = 1.5$, mesh M3 under *SRS* scheme: for variables (a) pressure, (b) velocity, (c) stress and (d) $D - D_c$.

in stress. Large amplitude oscillatory convergence patterns are observed in pressure, being larger for the larger time-steps, yet frequencies are similar. This is indicative of the improved temporal stability response with *incremental PC*. Comparatively, oscillatory patterns are reduced in velocity and smoothed in stress. In Fig. 4d, temporal evolution of the 'differed-correction term' is plotted, denoted as $(D - D_c)$ indicating its reduction through time. One may note that through this 'differed-correction term', temporal convergence rates follow faithfully those in stress, independent of time-step selection. Whilst achieving a steady state under a specified tolerance, this mechanism acts as a temporal control-monitor over solution evolution.

5.2. Stabilised schemes (CT3, TSS, RCI, and SRS), Ma = 0

The neutral incompressible *CT3*-scheme is the basis for comparative evaluation across the stabilisation techniques explored, and for conciseness, scheme acronyms are largely retained here. From Table 1, the *CT3*-scheme provides solutions up to the We_{crit} level of 2.8. The application of *Time-Step Stabilisation* alone has little influence on high-*We* stabilisation. Though a true-transient analysis may prove otherwise. We_{crit} attained is identical to that observed with *CT3*-scheme, reaching the same level of N_1-peak. The application of *Reduced Corner Integration* promotes We_{crit} from 2.8 (base-*CT3*) to 3.0. Clearly, introduction of the incompressible *SRS*-variant has promoted We_{crit} significantly, doubling its value from 2.8 (*CT3*) to 5.9. This finding lies in broad agreement with the observation of others who have employed similar strategies (see DEVSS/DG with GLS of Baaijens [6,19]).

5.2.1. Stress (τ_{xx}, τ_{xy}) profiles

These are illustrated in Fig. 5 through increasing *We* and scheme-variants plotted along the horizontal line along the

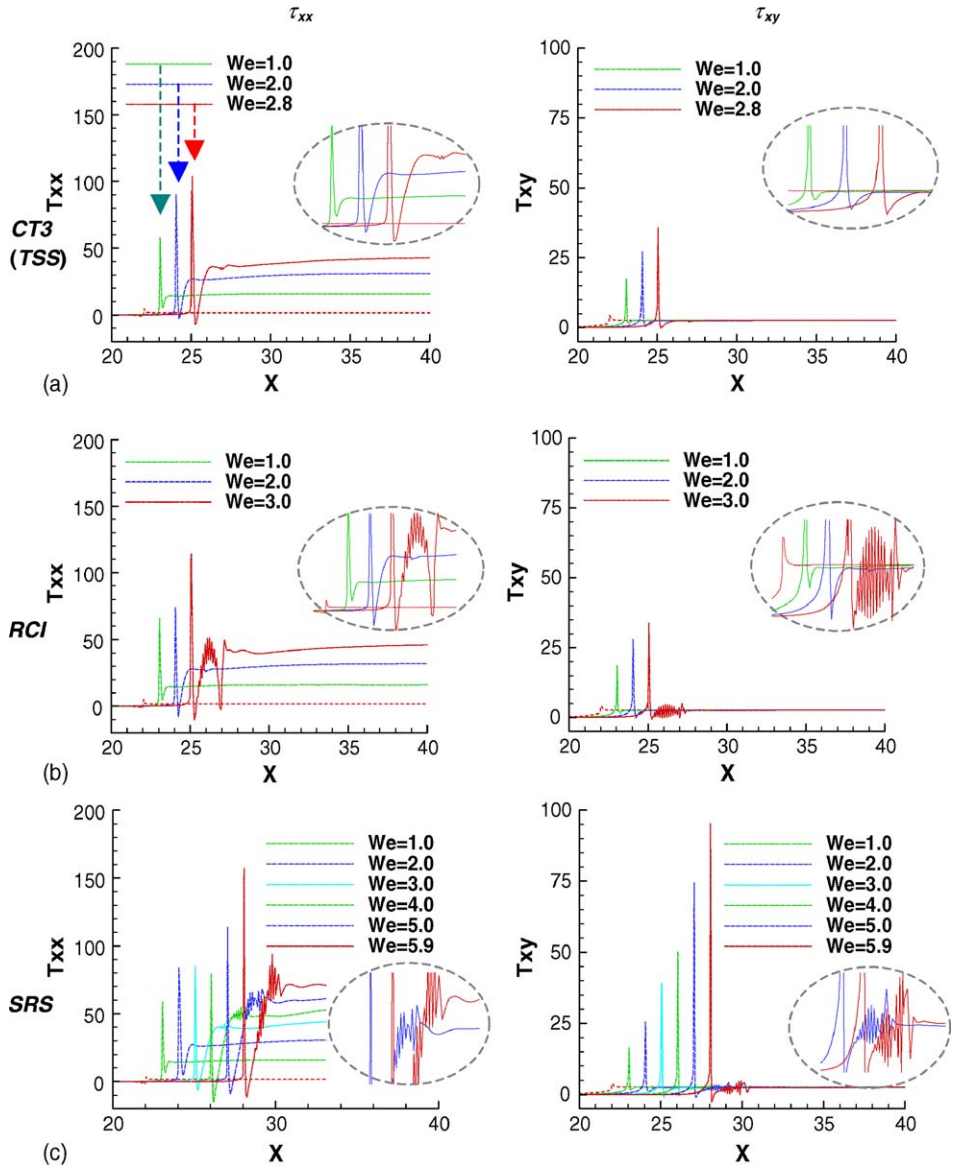

Fig. 5. $Ma = 0$ (τ_{xx}, τ_{xx})-profile, downstream-wall, increasing *We*: (left) τ_{xx} and (right) τ_{xy}; under schemes (a) *CT3*, (b) TSS, (c) *RCI* and (d) *SRS*.

downstream-wall ($y = 3.0$) at the level of the re-entrant corner. Note, in our comparative in-place presentation for stress profiles, we have applied a lateral shift for each *We*-solution plot, that displays a rising trend in peak values as *We* increases. There is a sharp rise in each stress component at the re-entrant corner to a peak and decay to a trough per *We*-solution. Beyond this state and in the τ_{xx} extensional stress, build-up is apparent to a *We*-dependent plateau level. Under *Time-Step Stabilisation*, stress profiles are identical to those of the *CT3*-scheme up to $We_{crit} = 2.8$, indicating that temporal stabilisation of this form does not impair scheme performance or affect the *CT3* steady-state solution. For *CT3* and *Time-Step Stabilisation* schemes, solution structure is practically oscillation-free, even at We_{crit}, as shown in Fig. 5a. Under *Reduced Corner Integration* in Fig. 5b at $We_{crit} = 3.0$, there is a 12% increase in τ_{xx} stress-peak compared to that with the *CT3*-scheme. Here, we observe large oscillations associated with the generation of a secondary vestigial stress-peak in both component profiles: an indicator of looming instability, largely absent at sub-critical *We*-levels. Stress (τ_{xx}, τ_{xy}) profiles with *Strain-Rate Stabilisation* of Fig. 5c display smooth patterns up to $We = 3.0$, that revert to oscillatory form beyond $We = 4.0$. Note, this level of *We* has not been attained by alternative scheme choices: *CT3*, TSS or *RCI*-schemes. Subsequently, these oscillatory patterns gather greater amplitude with increasing *We*, until ultimately this *Strain-Rate Stabilisation* version fails to converge beyond the super-elevated level of $We = 5.9$. At this *We*-level, the first normal stress N_1-peak value has risen to 133.4 units, representing an increase of some 46% above the corresponding value for *CT3*-scheme at $We_{crit} = 2.8$ (value 91.5 units). At $We = 3.0$, the vestigial peak found under *Reduced Corner Integration* is removed with *Strain-Rate Stabilisation*, where the solution is smooth and devoid of such features. We relate this response to the dissipative nature of the strain-rate treatment.

5.2.2. *Pressure and stress fields*

Next, for each scheme-alternative, we analyse pressure and stress (τ_{xx}, τ_{xy}) field plots within the contraction zone at sub-critical $We = 2.5$ (in Fig. 6) and We_{crit} (in Fig. 7). For $We = 2.5$ and *CT3*-scheme, Fig. 6a illustrates sharp gradients in the vicinity of the singular solution point and the downstream boundary layer. A comparison between *CT3* and *Time-Step Stabilisation* stress profiles and contours up to $We_{crit} = 2.8$ depicts no noticeable disparity. Henceforth, *Time-Step Stabilisation* results are withheld, replicating those of the *CT3*-form across all variables.

With *Reduced Corner Integration*, at $We = 2.5$ (Fig. 6b) and for higher *We* (Fig. 7b), oscillatory patterns begin to emerge in pressure and shear stress, close to and along the downstream-wall, in contrast to *CT3*-solutions. This is clear evidence of the *We* build-up of a stress boundary layer beyond the re-entrant corner, from which loss of stability results, concomitant with that reported in [29]. We comment that at $We = 2.0$, there are no oscillations apparent and solutions with *RCI* mimic those following the *CT3*-scheme (not shown). Primary elongational stress (τ_{xx}) remains relatively smooth on the field for all schemes up to We_{crit} (noting local profile behaviour as above). With respect to pressure and shear stress, trends are smoother with *Strain-Rate Stabilisation* when compared to *Reduced Corner Integration* forms (see Fig. 6c and d at $We = 2.5$). The oscillatory response within the boundary layer is particularly prominent in shear stress. Compared against *Reduced Corner Integration* solutions at $We_{crit} = 3.0$ (Fig. 7b), with *Strain-Rate Stabilisation* relatively smooth τ_{xy} patterns are extracted at $We = 4.5$ (Fig. 7c) and beyond in *We*. This position adjusts in approaching the limit

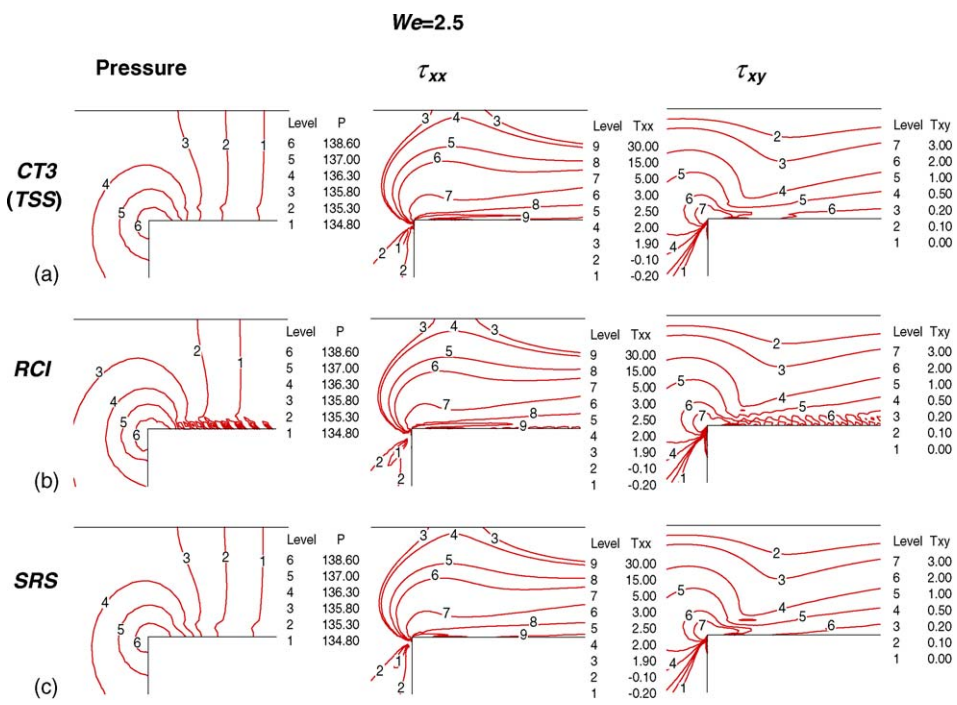

Fig. 6. $Ma = 0$ variable fields, $We = 2.5$: (left) pressure, (middle) τ_{xx} and (right) τ_{xy}; under schemes (a) *CT3*, (b) TSS, (c) *RCI* and (d) *SRS*.

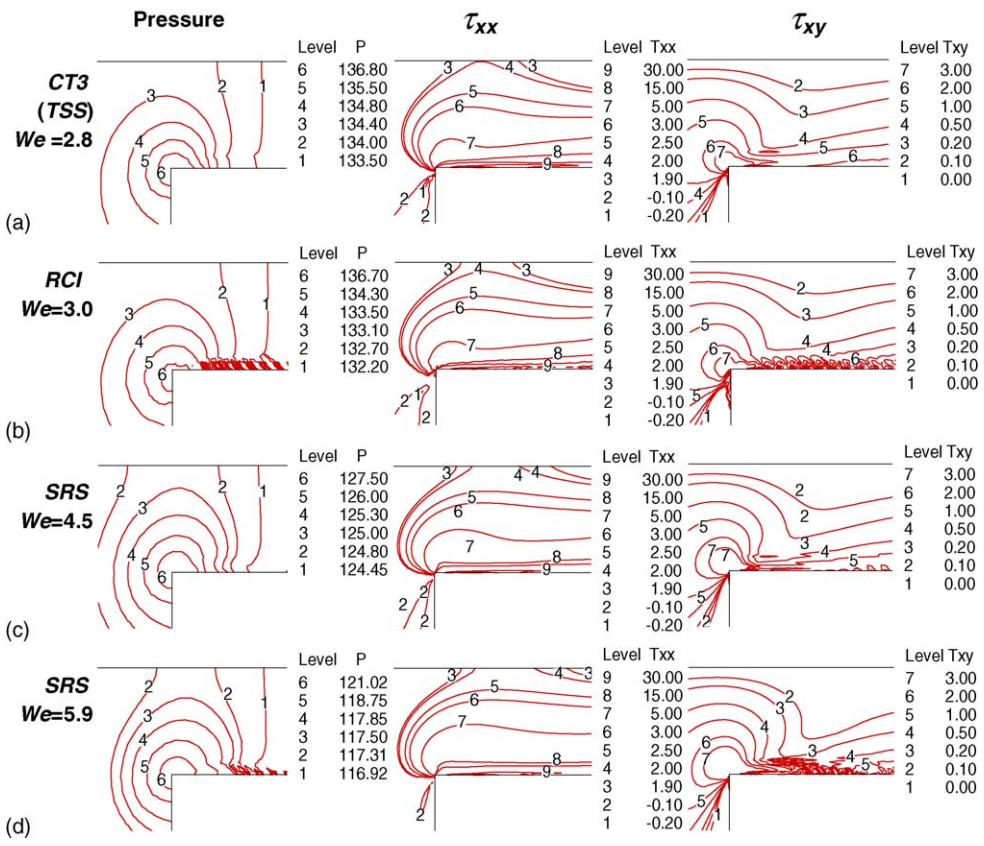

Fig. 7. $Ma = 0$ variable fields, large We: (left) pressure, (middle) τ_{xx} and (right) τ_{xy}; under schemes (a) *CT3*/TSS at $We_{crit} = 2.8$, (b) *RCI* at $We_{crit} = 3.0$, (c) *SRS* at $We = 4.5$ and (d) *SRS* at $We_{crit} = 5.9$.

$We_{crit} = 5.9$, when oscillations reappear in pressure and shear stress (Fig. 7d).

To identify the influence of *SRS* upon the flow field, steady-state three-dimensional plots of the $(D - D_c)$ term are provided in Fig. 8, at $We = 1.5$, 2.0 and 2.5 and $\Delta t = 5 \times 10^{-4}$. This figure starkly exposes the localised nature of the stabilisation term, which takes affect principally at the re-entrant corner in the form of a singular-valued function (usefully characterising the singularity). By increasing the We-level, the contribution of this term is slightly reduced through dissipation (by 30% from $We = 1.5$ through to $We = 2.5$). This evidence identifies that *SRS*-implementation does not disturb the solution field away from the localised re-entrant corner neighbourhood. Note that one may extract similar behaviour across schemes (*CT3* against *SRS*) at modest levels of We (problem-dependent), reflecting correspondence in vortex characteristics (see Fig. 14). We can infer that the influence of *SRS* is negligible when the solution is sufficiently smooth in the boundary layer. One may gather a connection to the use of dissipative terms in shock capturing, which are based on second- and fourth-order gradients of pressure. These terms become active near sharp gradients, yet are suppressed in smooth flow zones (see [30,31]).

5.2.3. *Velocity gradients and stress boundary layer*

Boundary layer analysis plays a key role in the understanding of viscoelastic flows near walls and corners. In Newtonian

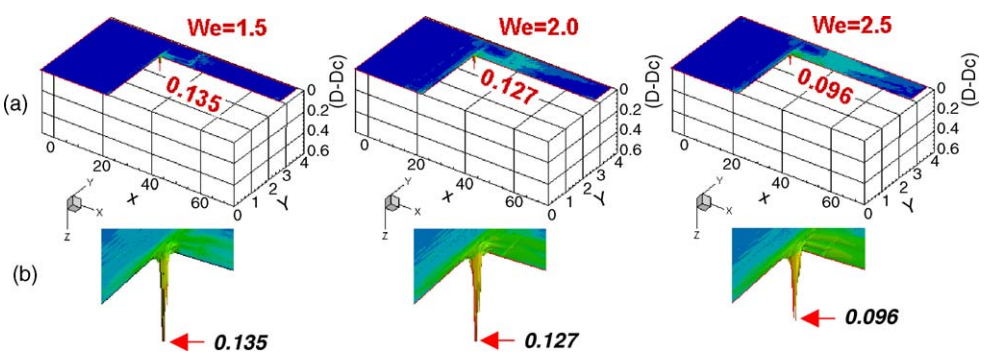

Fig. 8. $Ma = 0$ $(D - D_c)$ 3D-plots, increasing We; *SRS*-scheme, mesh M3: (a) whole domain, (b) re-entrant corner zone.

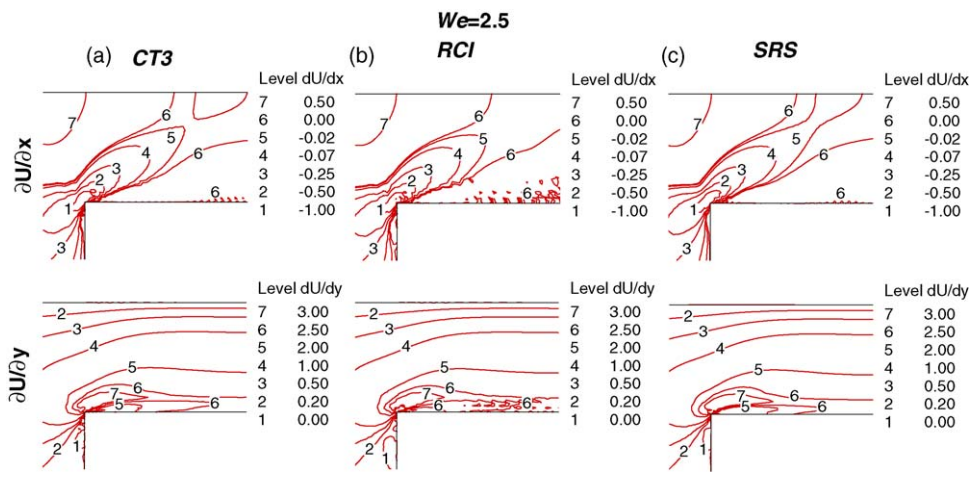

Fig. 9. $Ma = 0$ longitudinal velocity-gradient fields, $We = 2.5$: (top) streamwise $\partial u/\partial x$, (bottom) cross-stream $\partial u/\partial y$; under schemes (a) *CT3*, (b) *RCI* and (c) *SRS*.

flows, when inertial terms in the momentum equation are dominant, viscous terms may be neglected, except within thin fluid layers along no-slip solid boundaries. Stress boundary layers in the viscoelastic context are discussed in [32,33], and relevant references therein. Theoretically, stress boundary layer thickness is known to be proportional to We^{-1} for an Oldroyd-B model [29,34]. The effect of numerical noise within and across a thin stress boundary layer often poses severe discretisation and convergence difficulties. The resolution of these boundary layers has proved a major obstacle to successful viscoelastic computations at high *We*.

We proceed to clarify the dynamics of the stress boundary layer by interrogating the nature of the solution in the vicinity of the re-entrant corner and beyond, with back-reference to the discussion above on pressure and shear stress fields. We comment that the distortion noted in pressure field contours, beyond the re-entrant corner and across the stress boundary layer, vanishes as *We* reduces. This identifies that such distortion (away from level lines) is not due to a numerical pressure boundary layer, but rather to the consequence of the stress boundary layer itself. Correspondence amongst our results with *fe/fv*, and other *fv*-results in references [23,28,35], confirms consistency in predicted solutions across different schemes.

To extract the impact of the various terms on the stress boundary layer, in Fig. 9 velocity-gradient contour plots at $We = 2.5$ are presented for the principal schemes: *CT3*, *RCI* and *SRS*. This illustrates that the most active (largest) velocity-gradient component is $\partial u/\partial y$, being present in both τ_{xx}- and τ_{xy}-equations. Also, the numerical noise observed in $\partial u/\partial x$ (streamwise gradient) is highlighted, whilst the $\partial u/\partial y$ (transverse gradient) remains relatively smooth. Importantly, the accurate determination of this dominant ($\partial u/\partial y$) component strongly influences both τ_{xx}- and τ_{xy}-fields beyond the singular solution point, but more particularly τ_{xy}. As with the *CT3*-scheme in Fig. 9a, no oscillatory behaviour is observed and stress fields are consequently smooth. Equivalently, for the *RCI*-scheme, we observe degradation in velocity-gradient contours, as clearly demonstrated in Fig. 9b. Note that, at the lower level of $We = 2.0$, corresponding contours remain smooth. This may be a consequence of heavy oscillation within the τ_{xy}-field, noting that in comparison, the primary elongation stress τ_{xx} retains reasonable smoothness. The removal of numerical noise in Fig. 9c, indicates the enhanced stability of the *SRS*-scheme at this level of *We*, in contrast to that inherent within the *RCI*-implementation. Up to $We = 4.5$, the *SRS* stress contour plots retain smoothness (see Fig. 7c), beyond which oscillatory τ_{xy}-profiles emerge through the boundary layer.

Boundary layer evolution with increasing *We* is illustrated in Fig. 10 for the three variants, *CT3*, *RCI* and *SRS*-schemes. We characterise the profile of the stress boundary layer via the build up in entry-length (l) and detecting its outer perimeter through the vanishing $\partial\tau_{xx}/\partial y$ contour. In this fashion, build-up of the boundary layer in length is apparent with increasing *We* over each scheme, as annotated by arrow. The development of the boundary layer profile for the *CT3*-scheme is smooth up to $We_{crit} = 2.8$ (Fig. 10a). Around $We_{crit} = 3.0$ with the *RCI*-scheme, the boundary layer development has clearly become numerically 'polluted' and disjoint, as shown in Fig. 10b, reflecting once again oscillatory patterns in stress. Fig. 10c, provides further evidence of the enhanced stability, enjoyed with the *SRS*-scheme, through the evolution of the boundary layer with increasing *We* up to $We_{crit} = 5.9$. Hence, we see the consequence of *RCI*-adjustment is the propagation of noise into the downstream-wall stress boundary layer[2], generating oscillatory field patterns thereby (see [29]). In addition, we see below that *SRS* may be used as a mechanism to stabilise the *RCI*-strategy. Conversely, we would attribute the considerable elevation of We_{crit} under the *SRS*-implementation as being mainly due to the tight capturing of the stress boundary layer, via the inclusion of weak-form dissipative terms in the formulation, with factor $2\alpha\mu_s(D - D_c)$. This has the dual effect of controlling cross-stream solution prolongation, and at the same time, eases the compatibility relationship between function spaces adopted for velocity gradients and stress (also pressure, as a result).

[2] A link is established between lip-vortex activity stimulated and consequent degradation observed within the stress boundary layer, which may prove to be primarily responsible for subsequent failure in numerical convergence.

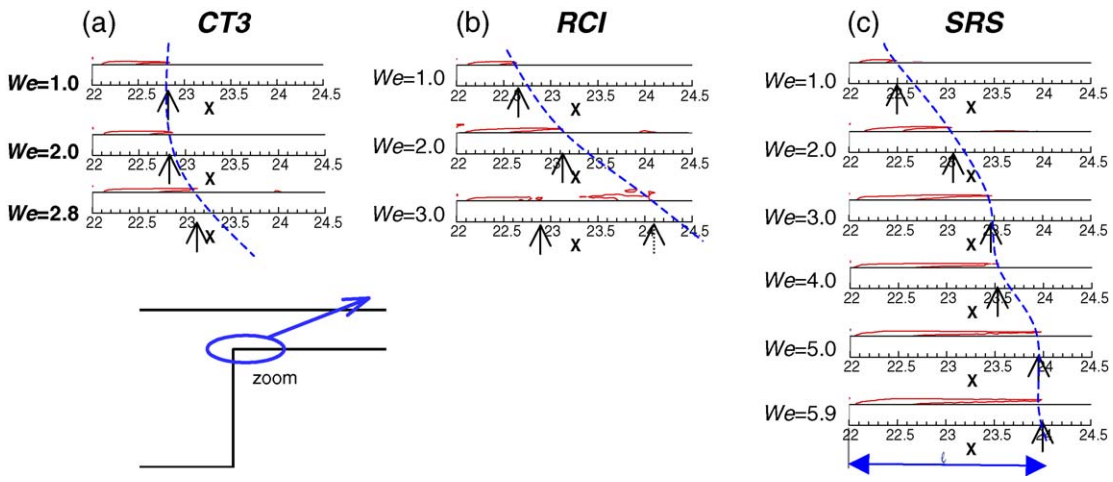

Fig. 10. $Ma = 0$ stress boundary layer characterisation, increasing We: under schemes (a) *CT3*, (b) *RCI* and (c) *SRS*.

5.3. Stabilised scheme combinations (RCI + SRS), Ma = 0

After investigating the effect of application of each individual stabilisation scheme when layered upon the incompressible *CT3*-variant, we are in a position to consider optimal scheme combinations. According to results tabulated in Table 1, the *RCI*-scheme has been found to produce heavy-side oscillation beyond $We = 2.5$ ($We_{crit} = 3.0$). Nevertheless, the stability properties of the *RCI*-scheme may be improved upon by appealing to combination with the *SRS*-scheme. This is demonstrated in stress profiles in Fig. 11, where prior *RCI*-oscillations, are now completely removed at $We = 3.0$. Oscillations appear once more at $We = 4.5$ and beyond, for the (*RCI* + *SRS*)-combination. Also, We_{crit} is progressively elevated from the level of 3.0 for the *RCI*-scheme, to 6.1 with the (*RCI* + *SRS*)-combination. We note from Table 1 that an all-scheme (*RCI* + TSS + *SRS*)-combination provides a remarkable level of $We = 6.4$. The benefit of *Strain-Rate Stabilisation* is again highlighted, in stabilising the numerical algorithm and promoting the We_{crit}-level crafted: the introduction of *Strain-Rate Stabilisation* has doubled We_{crit} over those forms without it. In Fig. 12, velocity-gradient profiles ($\partial u/\partial y$ and $\partial u/\partial y$) are contrasted at $We = 3.0$ on the downstream-wall

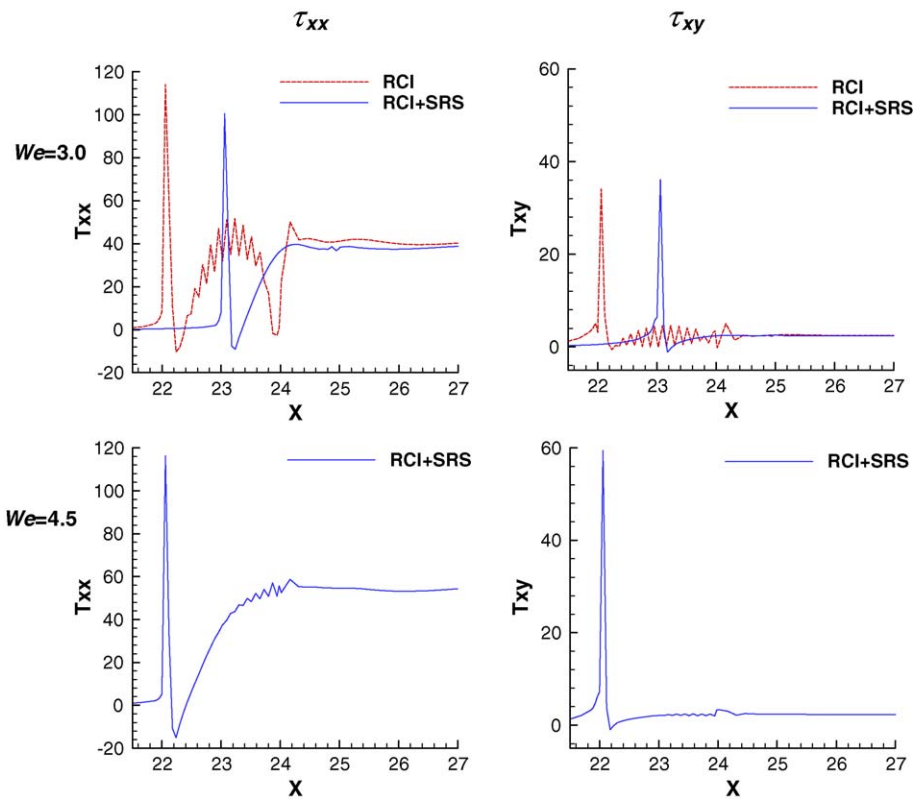

Fig. 11. $Ma = 0$ stress profiles, downstream-wall, scheme combinations: (left) τ_{xx} and (right) τ_{xy}; (top) $We = 3.0$, (middle) $We = 3.5$, and (bottom) $We = 4.5$.

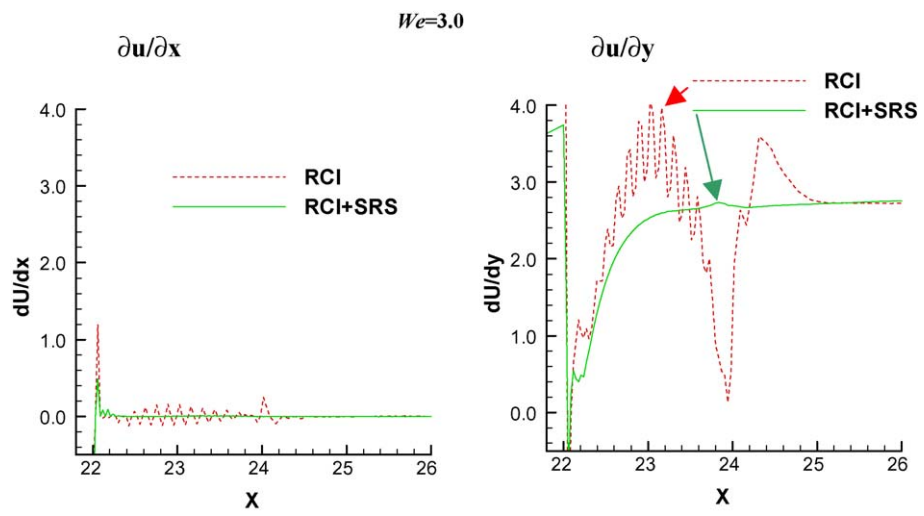

Fig. 12. Incompressible $\nabla\cdot u$-profiles, downstream-wall, *RCI*-scheme ± *SRS*-inclusion, $We = 3.0$: (left) streamwise $\partial u/\partial x$ and (right) cross-stream $\partial u/\partial y$.

horizontal line ($y = 3.0$) for *RCI* and (*RCI* + *SRS*)-variants. This figure illustrates the appearance of streamwise oscillations under *Reduced Corner Integration*, particularly prominent in the transverse gradient $\partial u/\partial y$ so vital to the accurate description of the stress boundary layer. Such oscillations are identified as being completely removed through combinations with *Strain-Rate Stabilisation*.

5.4. Limiting $Ma \to 0$ conditions: $Ma \approx 0$

To our knowledge and in the style adopted here, the consideration of compressibility effects in these viscoelastic flows is novel in this research area. In this limiting state, Tait parameters may be set to $(m, B) = (10^5, 10^5)$ with $Ma = O(10^{-5})$, hence emulating incompressible conditions (see extended Table 1).

5.4.1. $Ma \approx 0$ solutions alone

In contrast to $CT3_{Ma\approx 0}$-scheme ($We_{\text{crit}} = 2.0$) and Table 1 results, $RCI_{Ma\approx 0}$-scheme elevates We_{crit} to 3.3 and practically doubles N_1-peaks at respective We_{crit}. Likewise, $SRS_{Ma\approx 0}$-scheme promotes We_{crit} from 2.0 to 5.4, whilst maintaining the same $CT3_{Ma\approx 0}$-level of N_1-peak. *Strain-Rate Stabilisation* provides a major impact upon the $RCI_{Ma\approx 0}$-scheme (We_{crit} increases from 3.3 to 6.3 for $(RCI + SRS)_{Ma\approx 0}$), tripling We_{crit} for the $CT3_{Ma\approx 0}$-scheme. Here, *Strain-Rate Stabilisation* presence dominates to maintain the lowest levels of N_1-peak (observed say, at $We = 2.0$). The scheme with *Reduced Corner Integration* yet without *Strain-Rate Stabilisation* attains the largest N_1-peak levels, so that scheme combinations with both *RCI* and *SRS* are limited in N_1-peak between the bounds of each, as observed under the incompressible setting.

5.4.2. $Ma \approx 0$ versus $Ma = 0$

Here in Table 1, we compare compressible algorithm results against those with the conventional incompressible form. Overall, at a fixed $We = 2.0$ and under most schemes, we note elevated N_1-peaks with the $Ma \approx 0$-scheme, when compared to their $Ma = 0$-equivalents, as rationalised below. Correspondingly in We_{crit}, $CT3_{Ma\approx 0}$ and $SRS_{Ma\approx 0}$-results provide slightly lower values than their incompressible ($Ma = 0$) counterparts. Generally, the compressible '$\nabla\cdot u$' extra-term inclusion within the momentum equation has caused this reduction in We_{crit} (see below). Alternatively, the $RCI_{Ma\approx 0}$-scheme improves We_{crit} above that with the $RCI_{Ma=0}$-scheme (3.3 above 3.0), doubling N_1-peak values; this is also true for other *RCI*-combinations. This is due to the inherent mechanism of the *RCI*-scheme in handling sharp peaks.

5.4.3. Discarding '$\nabla\cdot u$' extra-term ($Ma \approx 0$)

We consider in greater detail the influence of the compressibility '$2/3 \times \nabla\cdot u$' term in Eq. (2), which vanishes under an incompressible ($Ma = 0$) setting (via $\nabla\cdot u \equiv 0$). As suggested by Oliveira and Pinho [36], this two-third term inclusion, taken in the constitutive equation for the incompressible setting, can improve numerical accuracy and steady-state convergence properties with *We* rise. This feature was observed in our previous work, for viscous liquid flows [3] and viscoelastic flows in [2], where the compressible algorithm with $Ma \approx 0$ displayed better *temporal* convergence characteristics over its incompressible alternative. To interrogate dependency and response to term inclusion under the compressible *CT3*-scheme, $Ma \approx 0$ setting, three numerical tests have been conducted. In the first, test (a), the 'conventional' incompressible scheme is employed for comparison ($\nabla\cdot u \equiv 0$ enforced). The second, test (b), consists of appending the extra-term to the momentum equation through Eq. (2) ($\kappa = 0$). In the third, test (c), this term is discarded, whilst the scheme remains compressible otherwise (equivalent to setting $\kappa = 2\mu_s/3$). A closer look at streamline patterns for $We = 2.0$ illustrated in Fig. 13a–c, shows that identical salient-corner vortex characteristics are obtained for each variant. However at this *We*-level, lip-vortex intensity is magnified some *four times* above the incompressible form under $Ma \approx 0$ setting (case (b)). The same level of lip-vortex intensity is observed for cases (a) and (c). Overall, this confirms that differences are localised to the re-entrant corner, affecting lip-vortex intensity and stress-peak levels, which have a direct influence on the

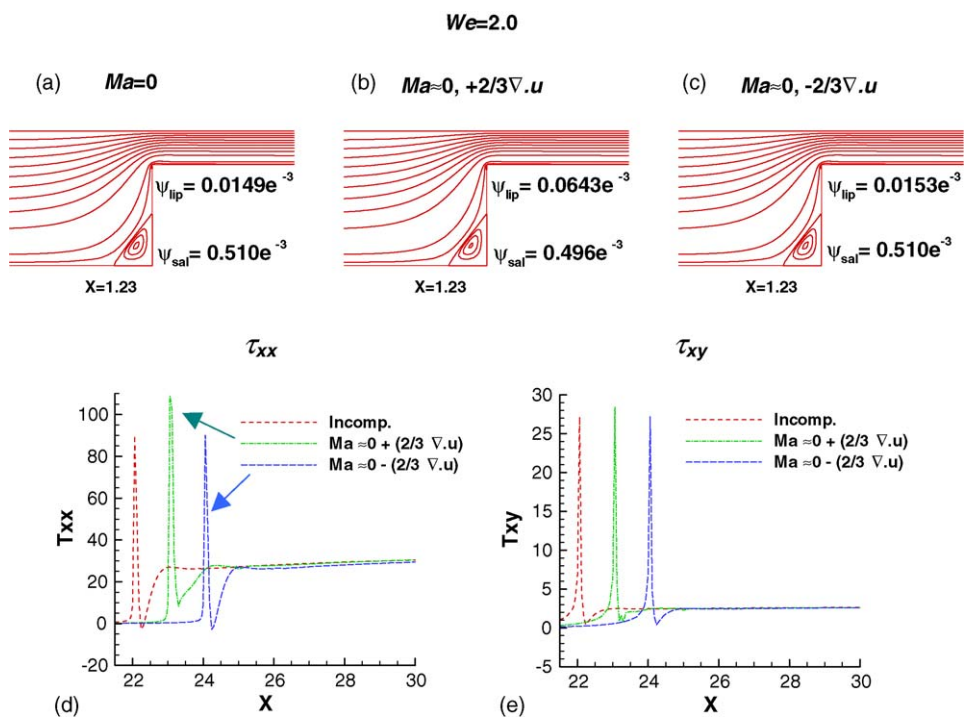

Fig. 13. '$\nabla\cdot u$' term influence, $We = 2.0$, *CT3*-scheme: stress profiles, downstream-wall: (a) τ_{xx}, (b) τ_{xy}, streamline patterns; (c) $Ma = 0$, no added term; (d) $Ma \approx 0$, added term; (e) $Ma \approx 0$, no added term.

level of We_{crit} reached. Findings are illustrated in Fig. 13d and e for $We = 2.0$, through stress (τ_{xx}, τ_{xy})-profiles and comparison against its true-incompressible counterpart (namely, case (a), $Ma = 0$). At $We = 2.0$, the extra-term inclusion has the effect of increasing stress-peak levels (particularly in τ_{xx}) by about 20% above the $Ma = 0$ case. Identical $Ma = 0$ solutions to the incompressible case are retrieved when the extra-term is nullified, with $We_{crit} = 2.8$ solution reached for case (c), mirroring that for incompressible case (a). For case (b), We_{crit} is lowered to 2.0 (as with $Ma = 0.1$ case). Hence, in the present algorithmic framework, we conclude that this extra-term inclusion for $Ma \approx 0$, is actually responsible for the early *loss of stability* beyond $We = 2.0$. The evidence is unequivocal. The extra inclusion of $\nabla\cdot u$ (continuity residual) alone is responsible for these flow features. Any local deterioration in continuity representation immediately impacts on lip-vortex generation.

6. Vortex behaviour

We proceed to enumerate our findings on vortex activity through finest mesh M3 solutions quantified via size, shape and strength, as a consequence of the additional stabilisation procedures outlined above. The literature base on vortex response of both salient-corner and lip-vortices is broad, being evidenced by works: experimentally, of Evans and Walters [37,38], McKinley et al. [39], and Boger [40]; and from simulation/theory, Matallah et al. [12], Aboubacar and Webster [9], Xue et al. [41], Oliveira and Pinho [36], Alves et al. [42], Renardy [29] and present authors [2,11]. Usefully, Alves et al. [28] and Aboubacar et al. [34,43] have catalogued many of the published results.

Fig. 14 provides a summary in the form of trend plots for our vortex activity results, displaying salient-corner vortex size and intensity (Fig. 14a and b), and lip-vortex intensity (Fig. 14c). In contrast to above and specific to vortex behaviour, we now cover both the incompressible limiting state ($Ma = 0$, $Ma \approx 0$) and the mildly compressible state ($Ma = 0.1$). Note, in all streamline plots, a total of 16 levels are dispatched, covering core-flow: 10 equitable levels, from 0.1 to 1.0, followed by levels at 10^{-2}, 10^{-3}; plus four levels to illustrate the salient-corner-vortex (inclusive from the minimum level to that of the separation-streamline). Here, the consideration of compressibility effects ($Ma = 0.1$) upon vortex activity in 4:1 contraction flows may be viewed as somewhat pioneering.

Under incompressible settings ($Ma = 0$ and $Ma \approx 0$), close agreement is observed amongst the various stabilisation strategies adopted and comparatively against the results of Alves et al. [28]. There is reduction in salient-corner vortex intensity towards a common threshold. The *CT3*-scheme displays a lip-vortex, and introducing *Reduced Corner Integration* constructs, under $Ma = 0$, promotes lip-vortex presence further (a trend upheld under $Ma \approx 0$). In contrast, *Strain-Rate Stabilisation* removes this flow feature completely. We may gather that this feature is linked directly to the numerical scheme and its treatment of the singularity.

In Fig. 15, $Ma = 0$-streamline contour plots for all scheme-variants are presented at $We = 2.0$ (left) and at We_{crit}-levels (right). Under the *CT3*-scheme and at lower *We*-levels, a large salient-corner vortex is present, both in size and intensity[3]; vor-

[3] No lip-vortex with *CT3* for $We < 2.0$; $\Psi_{sal} = -1.115 \times 10^{-3}$ at $We = 0.1$; $\Psi_{sal} = -0.838 \times 10^{-3}$ at $We = 1.0$.

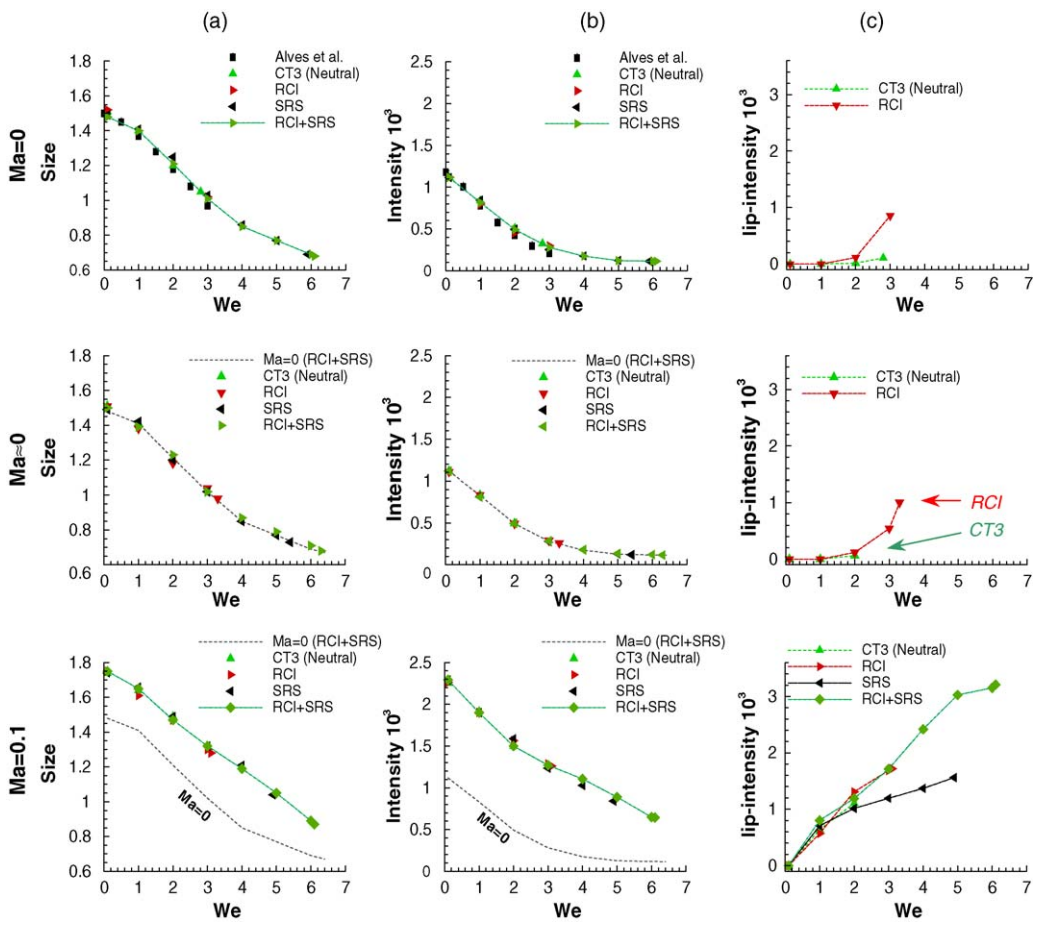

Fig. 14. Vortex trends, increasing *We*: (top) $Ma = 0.0$, (centre) $Ma \approx 0$, (bottom) $Ma = 0.1$; salient-corner vortex (a) size, (b) intensity and (c) lip-vortex intensity.

tex reduction is clearly apparent with increasing *We*. This trend of salient-corner vortex inhibition is observed for all stabilised schemes under consideration (identical size and intensity). With respect to the *CT3*-scheme (and *Time-Step Stabilisation*) and vortex activity, a minute lip-vortex appears at $We = 2.0$: intensity of 0.015×10^{-3}. This growth continues in intensity, to reach 0.107×10^{-3} at $We_{crit} = 2.8$. At $We = 1.5$, there is no indication of lip-vortex presence with either *CT3* or *Time-Step Scaling* schemes. Lip-vortex activity with the *RCI*-scheme is stimulated somewhat earlier at $We = 1.5$: intensity 0.095×10^{-3}. At $We = 2.0$, its intensity is about 1.5 times larger than its *CT3*-counterpart. Interestingly with $Ma = 0$, no lip-vortex is captured by any scheme with *Strain-Rate Stabilisation*, independent of *We*-level (see Fig. 15c and d). This issue shall be the subject of further analyses in subsequent work. It is conspicuous that, the *RCI*-scheme promotes lip-vortex activity when compared to other schemes.

All compressible stabilised scheme results reported in Fig. 14 with $Ma = 0.1$, $(m, B) = (4, 10^2)$, produce comparable salient-corner vortex characteristics as each other, lending further credence to correctness and precision. We observe larger salient-corner and lip-vortices in compressible flow above their incompressible counterparts, following similar evolution characteristics: salient-corner vortex-size decays with increasing *We* (vortex reduction), whilst lip-vortex size is enhanced. A well-developed compressible lip-vortex emerges as early as $We = 1.0$ and continues in its growth as *We* rises. Now, the compressible *SRS*-scheme does not remove the lip-vortex, as was the case under the incompressible setting (see above); yet there is some moderation of intensity in contrast to *CT3* and *RCI*-scheme results. Here, compressible versions of *RCI* or (*RCI* + *SRS*)-versions, promote the lip-vortex feature somewhat further in comparison to other scheme variants. The (*RCI* + *SRS*)-combination at large *We* develops a continuation of the *RCI*-lip-vortex trend.

Similarly, Fig. 16, compressible streamline plots for *CT3*, *RCI*, *SRS* and (*RCI* + *SRS*)-variants are presented at $We = 2.0$ (left) and at We_{crit}-levels (right) for each scheme. Here, we observe shape adjustment in salient-corner vortices from their equivalent incompressible form at $We = 0.1$ (same in the Newtonian case) to a more stretched, and convex form (separation line becomes curved). At $We = 2.0$, compressible salient-corner vortex characteristics are elevated compared to their incompressible forms by about 20% in size, tripling intensity. Similarly, on lip-vortex intensity and contrast between compressible to incompressible solutions across respective schemes: compressible *CT3* provides an intensity increase of two orders over incompressible *CT3*; compressible *RCI* equivalently gives an increase in intensity of one order over incompressible *RCI*. Notably any compressible implementation with *Strain-Rate Stabilisation* does

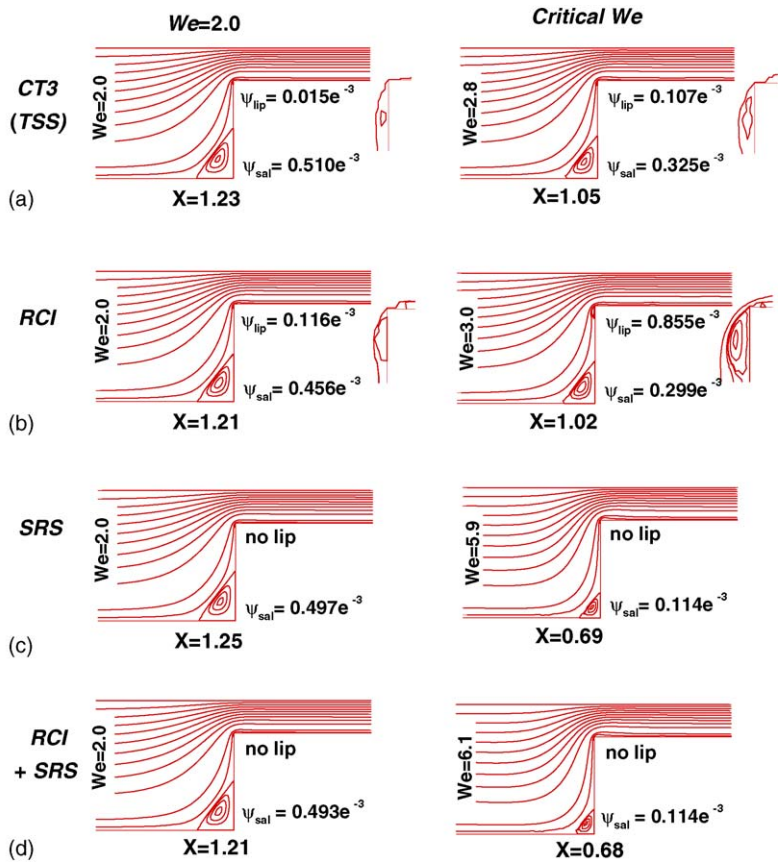

Fig. 15. $Ma = 0$ streamlines: (left) $We = 2.0$ and (right) We_{crit}; under schemes (a) *CT3*/TSS, (b) *RCI*, (c) *SRS* and (d) *RCI* + *SRS*.

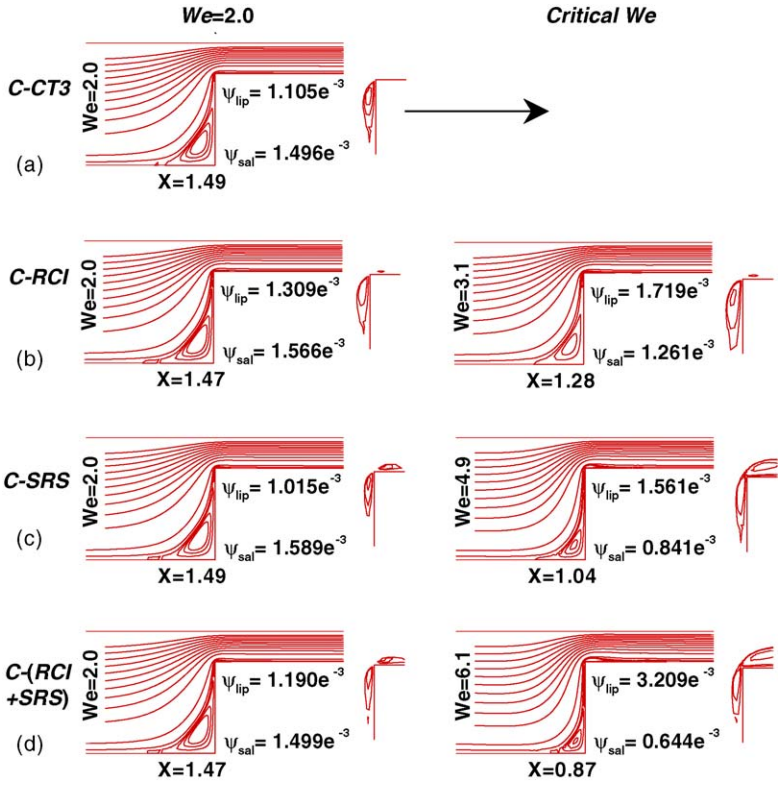

Fig. 16. $Ma = 0.1$ streamlines: (left) increasing We and $We = 2.0$, (right) We_{crit}; under schemes (a) C-*CT3*, (b) C-*RCI*, (c) C-*SRS* and (d) C-(*RCI* + *SRS*).

not remove the lip-vortex, as was the case under the incompressible setting. From $We = 3.0$-level onwards, we note that lip-vortex intensity becomes larger in absolute value than that of its salient-corner partner. At large *We*-level, the emergence of a second trailing-edge vortex on the downstream-wall, just beyond the re-entrant corner, is a specific feature new to the compressible setting.

7. Conclusions

This study has quantified the enhanced stabilisation characteristics of a time-marching incremental pressure-correction formulation, in solving the abrupt four-to-one planar contraction benchmark for Oldroyd-B viscoelastic flows. We have concentrated for the most part upon the limiting incompressible state. To do this, we have investigated *three* separate additional stabilisation strategies, embedded upon a hybrid *fe/fv*-implementation (base neutral scheme), reporting on levels of stable Weissenberg number solution; vortex activity, stress field structure about abrupt corners and in boundary layers; and cross-stream solution prolongation.

Temporal relaxation stabilisation applied through *Time-Step Stabilisation*, effective in a true transient scenario [2], is observed to have little relative influence in promoting steady-state high-*We* stability. In contrast, a second stabilisation strategy of *Reduced Corner Integration*, has promoted considerable stabilisation, particularly under compressible considerations. Under *Reduced Corner Integration*, large stress peaks have been extracted at the re-entrant corner, alongside large lip-vortex structures. Nevertheless, greatest improvement has been encountered with the third stabilisation strategy, *Strain-Rate Stabilisation*, for which We_{crit}-levels and stable solutions have more than doubled above those for the neutral variant. Theoretically, the weak dissipative term in the *Strain-Rate Stabilisation* formulation has the dual effect of: (i) controlling cross-stream solution propagation (absent in most currently favoured schemes) and (ii) easing compatibility relationships between function spaces on stress and velocity gradients (extended LBB-condition satisfaction). Here, stress peaks have been constrained, whilst lip-vortices have been completely removed under incompressible settings (with both $Ma = 0$ and $Ma \approx 0$). Combinations of these various stabilisation variants have recorded optimal stability properties. An unexpected result was that the *Strain-Rate Stabilisation* 'differed-correction term' ($D - D_c$) was found to characterise temporal error-norm stress convergence patterns; thereby also, the nature of the stress singularity at the re-entrant corner, yet without solution degradation elsewhere. Hence, this may be appreciated as a derived mechanism to incorporate singularity within the solution at the re-entrant corner. One may attribute the considerable elevation of We_{crit} under *Strain-Rate Stabilisation* to the tight capturing of the stress boundary layer accordingly.

Overall with increasing *We*, for each scheme and independent of flow conditions, we have observed salient-corner vortex reduction and lip-vortex growth. At a selected *We*-level and under a specific flow setting, all scheme variants have produced similar salient-corner vortex trends. In contrast, lip-vortex features are found to be significantly affected by the particular re-entrant corner treatment. Surprisingly, at incompressible ($Ma = 0$ and $Ma \approx 0$) levels, we have observed that continuity residual error may spark off lip-vortex response. This generates exaggerated re-entrant corner stress peaks that distinguish between ($Ma = 0$) and ($Ma \approx 0$) solutions. The absence of lip-vortices under the same conditions with *Strain-Rate Stabilisation* has clearly identified this position. Nevertheless, this lip-vortex feature is certainly present under the mildly compressible $Ma = 0.1$ setting, with or without *Strain-Rate Stabilisation*. The relaxation of the incompressible constraint has therefore proved responsible for identifying such anomalies, which are laid bear at the discrete level. This leaves some open questions of general algorithms/codes and of the quality of their respective solution representations about such singularities (degradation in local continuity residual). This lays still greater demands upon localised mesh resolution and convergence thresholds to more precisely approximate steady-state and transient dynamics.

Acknowledgement

The EPSRC financial support (GR/R46885/01) is gratefully acknowledged.

Appendix A. Mildly compressible scheme performance; $Ma = 0.1$

For completeness and in contrast to the incompressible setting, we include our summarised findings on scheme performance across schemes for the mildly *compressible setting with $Ma = 0.1$, using $(m, B) = (4, 10^2)$. Such a *Ma*-level leads to an exaggerated rise in density, of about 30% above that experienced in an equivalent incompressible flow. Table A1 covers We_{crit} and first normal stress-peak $N_1 = (\tau_{xx} - \tau_{yy})$ levels reached for each compressible scheme variant: C-*CT3*, C-*RCI*, C-*SRS*, C-(*RCI* + *SRS*). The neutral C-*CT3* scheme achieved $We_{\text{crit}} = 2.0$. This level is promoted to $We_{\text{crit}} = 3.1$ under *Reduced Corner Integration* methodology. *Strain-Rate Stabilisation* is the most effective elevating the We_{crit} level above that for C-*CT3* by some 2.5 times, whilst with the C-(*RCI* + *SRS*)-combination, this has more than tripled We_{crit} to 6.1. For each compressible scheme, we observe a lowering of We_{crit} by about a unit below its incompressible correspondent (see Table 1 with $Ma = 0$, one reason for which may be $\nabla \cdot u$ inclusion). That is, with the exception

Table A1
Compressible setting (Ma = 0.1): Wecrit and principal stress-peak N_1, various schemes

	$Ma = 0.1$			
	Alone			Combination
	C-*CT3*	C-*RCI*	C-*SRS*	C-(*RCI* + *SRS*)
Critical *We*	2.0	3.1	4.9	6.1
Peak N_1 at We_{crit}	99.1	200.8	107.6	183.5
N_1 at $We = 2.0$	99.1	122.8	73.4	73.5

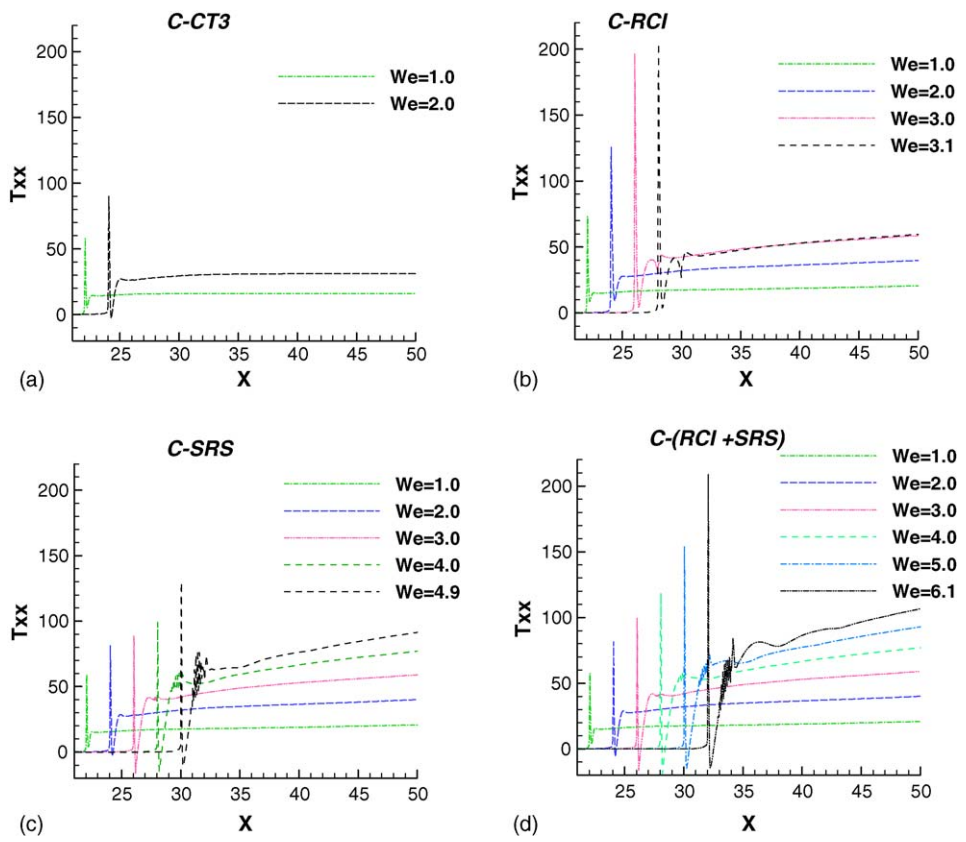

Fig. A1. $Ma = 0.1$ τ_{xx}-profiles, downstream-wall, increasing *We*: under schemes (a) C-*CT3*, (b) C-*RCI*, (c) C-*SRS* and (d) C-(*RCI* + *SRS*).

of *Reduced Corner Integration* schemes, where We_{crit} levels are maintained; with these schemes additional properties are imbued to handle steep corner-gradients. With regard to N_1-peak at a selected *We*-level, *Strain-Rate Stabilisation* displays the lowest value, whilst *Reduced Corner Integration* claims the largest.

Compressible longitudinal stress τ_{xx}-profiles are illustrated along the downstream-wall in Fig. A1 through increasing *We* for these compressible schemes. After the re-entrant corner, we observe monotonic streamwise τ_{xx} stress build-up along the solid wall. The growth rate of τ_{xx} along the downstream-wall increases as *We* increases (initial rate/angle in radians for $Ma = 0.1$, empirically estimated as a function of We^k, $k_{C\text{-}(RCI+SRS)} = 0.36$). This characteristic is attributed to the velocity field and observed only under the compressible τ_{xx} setting; it reflects the dependence upon density (see Eq. (6a)) which impacts upon the stress field accordingly. Furthermore at $We = 2.0$, *Strain-Rate Stabilisation* variants maintain their τ_{xx}-peak levels, within 5%, of their respective incompressible values. At the same $We = 2.0$ level, the compressible τ_{xx}-peak for *CT3* rises by 20% for compressible above incompressible variants (see Figs. 5 and A1). From Fig. A1, at $We = 2.0$ and $We = 3.0$, *Reduced Corner Integration* has smoothed τ_{xx} stress profiles and doubled stress-peaks over incompressible equivalents. With compressible *Strain-Rate Stabilisation*, smaller oscillations are observed in comparison to its incompressible counterpart at $We = 3.0$ and stronger stability is enjoyed up to $We_{crit} = 4.9$; though oscillations are amplified between these two *We*-levels. At $We_{crit} = 4.9$ the C-*SRS* scheme τ_{xx}-peak is some 8% larger than that for C-*CT3* scheme at $We_{crit} = 2.0$. The response on We_{crit} under the C-(*SRS* + *RCI*)-combination is an impressive level of $We_{crit} = 6.1$.

Correspondingly, we present in Fig. A2, compressible field results through τ_{xy}-contours with rising *We* over $We = 2.0$, 3.0, 4.5 and 5.5. This demonstrates that the lack of smoothness in C-(*RCI* + *SRS*)-solutions is delayed in appearance to beyond $We = 4.5$. Around the contraction zone is a region of low *Ma*. There, we observe little difference in compressible pressure and stress fields, in comparison to their incompressible alternatives. Here, we may recall the irregularity in incompressible τ_{xy}-fields at large *We*-levels. Under *Reduced Corner Integration* constructs, we note the smooth structure gathered for the compressible setting in contrast to its incompressible counterpart (see Figs. 6 and 7). In addition, under the C-*RCI* scheme, velocity-gradient fields are smooth, whilst τ_{xx}-fields are smooth for all $Ma = 0.1$-variants (as for $Ma = 0$). Along the downstream-wall, the compressible stress boundary layer is a region subject to relatively low *Ma*-levels (typically, $Ma < 0.001$). Therefore, compressibility has little impact upon this stress boundary layer. Hence, stress boundary layer development under compressible conditions follows that of its incompressible counterpart. With respect to *Reduced Corner Integration*, the compressible solution maintains smoothness up to $We_{crit} = 3.1$ and the stress boundary layer for this *We*-level is also smooth (see its incompressible counterpart at $We = 3.0$).

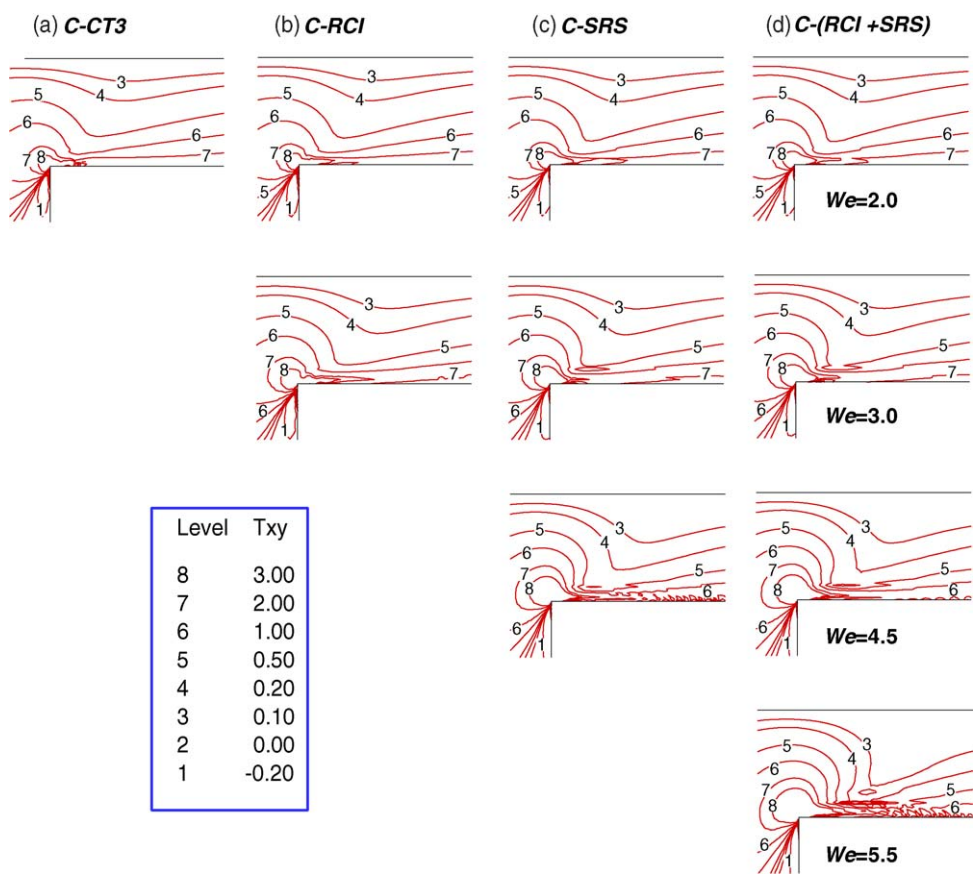

Fig. A2. $Ma = 0.1\tau_{xy}$-fields, $We = 2.0$–5.5: under schemes (a) C-*CT3*, (b) C-*RCI*, (c) C-*SRS* and (d) C-(*RCI* + *SRS*).

References

[1] K. Walters, M.F. Webster, The distinctive CFD challenges of computational rheology, Int. J. Numer. Meth. Fluids 43 (2003) 577–596.
[2] I.J. Keshtiban, F. Belblidia, M.F. Webster, Numerical simulation of compressible viscoelastic liquids, J. Non-Newtonian Fluid Mech. 122 (2004) 131–146.
[3] M.F. Webster, I.J. Keshtiban, F. Belblidia, Computation of weakly-compressible highly-viscous liquid flows, Eng. Comput. 21 (2004) 777–804.
[4] M.F. Webster, H.R. Tamaddon-Jahromi, M. Aboubacar, Time-dependent algorithm for viscoelastic flow-finite element/volume schemes, Numer. Meth. Partial Diff. Eqn. 21 (2005) 272–296.
[5] R. Keunings, Simulation of viscoelastic flow, in: C.L. Tucker (Ed.), Proceedings of the Computer Modeling for Polymer Processing Conference, 1989, pp. 404–469.
[6] F.P.T. Baaijens, Mixed finite element methods for viscoelastic flow analysis: a review, J. Non-Newtonian Fluid Mech. 79 (1998) 361–385.
[7] R. Codina, O.C. Zienkiewicz, CBS versus GLS stabilization of the incompressible Navier–Stokes equations and the role of the time step as stabilization parameter, Comm. Numer. Meth. Eng. 18 (2002) 99–112.
[8] J.L. Guermond, L. Quartapelle, On stability and convergence of projection methods based on pressure Poisson equation, Int. J. Numer. Meth. Fluids 26 (1998) 1039–1054.
[9] M. Aboubacar, M.F. Webster, A cell-vertex finite volume/element method on triangles for abrupt contraction viscoelastic flows, J. Non-Newtonian Fluid Mech. 98 (2001) 83–106.
[10] T. De Mulder, The role of bulk viscosity in stabilized finite element formulations for incompressible flow: a review, Comp. Meth. Appl. Mech. Eng. 163 (1998) 1–10.
[11] F. Belblidia, I.J. Keshtiban, M.F. Webster, Stabilised computations for incompressible and mildly compressible viscoelastic flows, Report No. CSR 01-2005, Computer Science Department, University of Wales Swansea, UK. http://www-compsci.swan.ac.uk/reports/.
[12] H. Matallah, P. Townsend, M.F. Webster, Recovery and stress-splitting schemes for viscoelastic flows, J. Non-Newtonian Fluid Mech. 75 (1998) 139–166.
[13] E.O.A. Carew, P. Townsend, M.F. Webster, A Taylor–Petrov–Galerkin algorithm for viscoelastic flow, J. Non-Newtonian Fluid Mech. 50 (1993) 253–287.
[14] P. Wapperom, M.F. Webster, Simulation for viscoelastic flow by a finite volume/element method, Comp. Meth. Appl. Mech. Eng. 180 (1999) 281–304.
[15] J.M. Marchal, M.J. Crochet, A new mixed finite element for calculating viscoelastic flow, J. Non-Newtonian Fluid Mech. 26 (1987) 77–114.
[16] F.G. Basombrio, G.C. Buscaglia, E.A. Dari, Simulation of highly elastic fluid flows without additional numerical diffusivity, J. Non-Newtonian Fluid Mech. 39 (1991) 189–206.
[17] F. Brezzi, M. Fortin, Mixed and Hybrid Finite Elements Methods, Springer-Verlag, New York, 1991.
[18] M. Fortin, A. Fortin, A new approach for the FEM simulation of viscoelastic flows, J. Non-Newtonian Fluid Mech. 32 (1989) 295–310.
[19] F.P.T. Baaijens, An iterative solver for the DEVSS/DG method with application to smooth and non-smooth flows of the upper convected Maxwell fluid, J. Non-Newtonian Fluid Mech. 75 (1998) 119–138.
[20] O.C. Zienkiewicz, J.Z. Zhu, The superconvergent patch recovery and a posteriori error estimates. Part 1. The recovery technique, Int. J. Numer. Meth. Eng. 33 (1992) 1331–1364.
[21] J. Sun, N. Phan-Thien, R.I. Tanner, An adaptive viscoelastic stress splitting scheme and its applications: AVSS/SI and AVSS/SUPG, J. Non-Newtonian Fluid Mech. 65 (1996) 75–91.

[22] H. Matallah, P. Nithiarasu, M.F. Webster, Stabilisation techniques for viscoelastic flows, in: Proceedings of the ECCOMAS Conference, 2001.
[23] M. Aboubacar, T.N. Phillips, H.R. Tamaddon-Jahromi, B.A. Snigerev, M.F. Webster, High-order finite volume methods for viscoelastic flow problems, J. Comput. Phys. 199 (2004) 16–40.
[24] R. Guénette, M. Fortin, A new mixed finite element method for computing viscoelastic flows, J. Non-Newtonian Fluid Mech. 60 (1995) 27–52.
[25] W.M.H. Verbeeten, G.W.M. Peters, F.P.T. Baaijens, Numerical simulations of the planar contraction flow for a polyethylene melt using the XPP model, J. Non-Newtonian Fluid Mech. 117 (2004) 73–84.
[26] I.J. Keshtiban, F. Belblidia, M.F. Webster, Computation of incompressible and weakly-compressible viscoelastic liquids flow: finite element/volume schemes, J. Non-Newtonian Fluid Mech. 126 (2005) 123–143.
[27] M.F. Webster, H.R. Tamaddon-Jahromi, M. Aboubacar, Transient viscoelastic flows in planar contractions, J. Non-Newtonian Fluid Mech. 118 (2004) 83–101.
[28] M.A. Alves, P.J. Oliveira, F.T. Pinho, Benchmark solutions for the flow of Oldroyd-B and PTT fluids in planar contractions, J. Non-Newtonian Fluid Mech. 110 (2003) 45–75.
[29] M. Renardy, Current issues in non-Newtonian flows: a mathematical perspective, J. Non-Newtonian Fluid Mech. 90 (2000) 243–259.
[30] E.O.A. Carew, P. Townsend, M.F. Webster, On a discontinuity capturing technique for Oldroyd-B fluids, J. Non-Newtonian Fluid Mech. 51 (1994) 231.
[31] A. Jameson, W. Schmidt, E. Turkel, Numerical solutions of the Euler equations by finite volume methods using Runge–Kutta time-stepping schemes, in: AIAA, Proceedings of the 14th Fluid and Plasma Dynamic Conference, 1981, pp. 1259–1276.
[32] J.M. Rallison, E.J. Hinch, The flow of an Oldroyd fluid past a re-entrant corner: the downstream boundary layer, J. Non-Newtonian Fluid Mech. 116 (2004) 141–162.
[33] T. Hagen, M. Renardy, Boundary layer analysis of the Phan–Thien–Tanner and Giesekus model in high Weissenberg number flow, J. Non-Newtonian Fluid Mech. 73 (1997) 181–189.
[34] M. Aboubacar, H. Matallah, M.F. Webster, Highly elastic solutions for Oldroyd-B and Phan–Thien/Tanner fluids with a finite volume/element method: planar contraction flows, J. Non-Newtonian Fluid Mech. 103 (2002) 65–103.
[35] S.S. Edussuriya, A.J. Williams, C. Bailey, A cell-centred finite volume method for modelling viscoelastic flow, J. Non-Newtonian Fluid Mech. 117 (2004) 47–61.
[36] P.J. Oliveira, F.T. Pinho, Plane contraction flows of upper convected Maxwell and Phan–Thien–Tanner fluids as predicted by a finite-volume method, J. Non-Newtonian Fluid Mech. 88 (1999) 63–88.
[37] R.E. Evans, K. Walters, Flow characteristics associated with abrupt changes in geometry in the case of highly elastic liquids, J. Non-Newtonian Fluid Mech. 20 (1986) 11–29.
[38] R.E. Evans, K. Walters, Further remarks on the lip-vortex mechanism of vortex enhancement in planar-contraction flows, J. Non-Newtonian Fluid Mech. 32 (1989) 95–105.
[39] G.H. McKinley, W.P. Raiford, R.A. Brown, R.C. Armstrong, Nonlinear dynamics of viscoelastic flow in axisymmetric abrupt contractions, J. Fluid Mech. 223 (1991) 411–456.
[40] D.V. Boger, Viscoelastic flows through contractions, Annu. Rev. Fluid Mech. 19 (1987) 157–182.
[41] S.-C. Xue, N. Phan-Thien, R.I. Tanner, Three dimensional numerical simulations of viscoelastic flows through planar contractions, J. Non-Newtonian Fluid Mech. 74 (1998) 195–245.
[42] M.A. Alves, F.T. Pinho, P.J. Oliveira, Effect of a high-resolution differencing scheme on finite-volume predictions of viscoelastic flows, J. Non-Newtonian Fluid Mech. 93 (2000) 287–314.
[43] M. Aboubacar, H. Matallah, H.R. Tamaddon-Jahromi, M.F. Webster, Numerical prediction of extensional flows in contraction geometries: hybrid finite volume/element method, J. Non-Newtonian Fluid Mech. 104 (2002) 125–164.